Bank Effects for KVLCC2

Wim Van Hoydonck[1], Serge Toxopeus[2] (AM)**, Katrien Eloot[1,3], Karan Bhawsinka[2], Patrick Queutey[4] and Michel Visonneau[4]**
[1] Flanders Hydraulics Research (FHR), Antwerp, Belgium
[2] Maritime Research Institute Netherlands (MARIN), Wageningen, the Netherlands
[3] Maritime Technology Division, Ghent University, Ghent, Belgium
[4] CNRS, LHEEA Lab. (ECN/CNRS), Nantes, France

A study is presented on ship-bank interaction effects in which viscous-flow solvers are used to predict the hydrodynamic forces and moments on the ship. The ship under consideration is the KRISO Very Large Crude Carrier (KVLCC2). For this hull form, Flanders Hydraulics Research (FHR) has conducted shallow water model tests in their towing tank equipped with surface-piercing banks and a vertical quay wall. The forces and moments on the KVLCC2 model were obtained for various water depths and lateral distances to the banks. Additionally, the wave elevation was measured between the quay wall and the ship model. In this study, two different CFD codes are used to predict the loads on the KVLCC2 as a function of the water depth and position in the channel. The effect of propeller suction and free surface modelling on the results is quantified. Furthermore, results are compared with potential flow computations to highlight the benefits of each approach. Additionally, comparisons will be made with CFD results from literature. The paper will show that with careful setup of the computations, reliable predictions of the ship-bank interaction effects can be obtained.

KEYWORDS
KVLCC2; bank suction; ship-bank interaction; manoeuvring; CFD; potential flow

INTRODUCTION
Ship-bank interaction is an important effect on vessels sailing in waterways. It is important to account for these interaction effects in nautical training programs and in engineering analyses because interaction forces can be large and dynamic in nature. These effects can change abruptly and lead to a ship unexpectedly deviating from its original course and consequently, they can influence the nautical accessibility inside ports, access channels and locks.

It is common practice to compute ship-bank interaction using model tests (Dand 1981; Vantorre and Laforce 1998; Lataire et al. 2012) or off-line computations using hydrodynamic models ranging from strip-theory-based interaction models to double-body potential flow using panel models. Tuck and Newman (1974) developed two theories. First, they used slender body theory to calculate hydrodynamic interaction forces between two encountering ships moving at constant (but possibly different) velocity. In the second case, the effects of shallow water were considered when the vessels were moving with the same velocity. The developed theories gave excellent qualitative and fair quantitative agreement with experimental results. Yeung and Tan (1980) investigated hydrodynamic interactions of a slow moving vessel with a coastline or an obstacle in shallow water using slender-body theory. Results were not compared with any experimental data. Pinkster and Bhawsinka (2013) developed a computational procedure for ship-ship and ship-port structure interaction using a double-body potential flow method and applied it to a real-time manoeuvring simulator. It was concluded that, after tuning with model test results, the computational procedure gives reliable computation of interaction forces enabling users of real-time simulators to simulate wider ranges of distances and speeds between passing structures. Zhou and Z. Zou (2013) use a first-order Rankine source panel method to predict the squat of a ship sailing in restricted waters. The method takes the free surface into account. To improve results, a virtual extension of the transom is generated and added to the length of the vessel. Results are compared to experimental values published in Lataire et al. (2012) and empirical formulas. The authors find that the method can be applied for ship squat prediction as long the ship is not close to the bank.

All the computational procedures listed above ignore free surface effects (except for Zhou and Z. Zou (2013)) and viscous effects while calculating interaction forces. Therefore, results from these methods start to deviate from reality at high speeds and at large drift angles (Bunnik and Toxopeus 2011). Furthermore, none of these methods take into account the effect of propeller RPM on interaction forces which are known to be significant, especially when the ship is sailing in close proximity to another structure.

More recently, attempts have been made to obtain these interaction forces using CFD computations. As CFD methods can account for free surface, viscous effects and propeller RPM while calculating interaction forces, this seems like a logical next step. Chen et al. (2003) used an unsteady chimera RANS method to study the ship-ship interaction problem in shallow and restricted waterways and validated the method against some available experimental measurements. The computed interaction forces and moments matched very well with the experimental results. They also investigated the importance of including the free surface, sinkage and trim and the influence of wall boundary conditions. Lo et al. (2009) applied FLOW-3D CFD software to simulate

bank effect on the KRISO 3600 TEU container ship model. Their results state that CFD modelling has achieved high precision to simulate bank effects without the need for conducting extensive model tests. L. Zou et al. (2011), L. Zou (2012), and L. Zou and Larsson (2013) have done significant work in this field recently. They utilised CFD methods to investigate bank effects on a tanker moving straight ahead at low speed in a canal characterised by surface-piercing banks. Their work includes verification and validation based on a grid convergence study and comparison with experimental data, as well as the exploration of modelling error in RANS computations to enable more accurate and reliable predictions of the bank effects. In general, the CFD results of this work were considered promising and compared well with experimental data. It should be noted that L. Zou and Larsson (2013) seem to provide the first publication where the effect of propeller RPM on bank suction forces were analysed using CFD. It is concluded that the propeller increases the velocity around the aft-body, just like in unrestricted flow, but due to the very low velocities on the starboard (vertical wall) side, this half of the propeller gets more heavily loaded. It therefore sucks more flow on the starboard side and the reduced pressure causes a bow-out moment on the hull with the rotating propeller.

In the present paper, work performed within the NATO Science and Technology Organization (STO) AVT-216 working group is presented. Experiments conducted at Flanders Hydraulics Research (FHR) with a 1/75 scale model of the KVLCC2 have been reproduced with two viscous-flow solvers and one potential flow solver in order to evaluate the prediction capability of these tools regarding bank effects. Earlier publications in which these FHR experiments were studied only provided a qualitative discussion on the agreement with the experiments. The present paper will present quantitative comparisons with the experimental forces and moments. The effects of free surface modelling and the influence of the propeller on bank effects will be discussed to highlight modelling sensitivities in the results.

EXPERIMENTAL DATA

Towing tank facility

The tests with bank configuration have been carried out in the towing tank for manoeuvres in shallow water, located at Flanders Hydraulics Research and administrated in cooperation with the Maritime Technology Division of Ghent University on 22, 27, 28 and 29 May 2010. The particulars and possibilities of this towing tank have been extensively described in Van Kerkhove et al. (2009). A short summary is given below.

Experimental setup

Towing tank dimensions The main dimensions of the towing tank are listed in Table 1.

Ship model FHR owns a 1/75 scale model of the KRISO Very Large Crude carrier (KVLCC2), which was built according to the lines provided by SIMMAN (2nd variant). Consequently, its main particulars including propeller data, can be found on the SIMMAN website[1]. The hydrostatic dependent particulars are given in Table 2 for the bank effects test program. The centre of gravity of the ship is located on the waterline.

Water depths The ship model was tested at the water depths listed in Table 3. The respective under keel clearance (UKC) values are listed here as well, as are the names of the test sequences.

Bank Geometry The towing tank is equipped with a double bank configuration along the full length of the tank. An overview of the towing tank with banks is shown in Figure 1. During the tests, the ship model sails from the far side to the front of the basin. The first part of the tank that the model encounters is equipped with a $1/1$ sloped wall on the negative side and a $1/3$ slope on the positive side. The second section ($0 < x < 34\,\mathrm{m}$ in basin coordinates) contains a vertical wall (at $-2.7\,\mathrm{m}$) on the negative side and on the positive side a bank with a slope of $1/4$. A cross section of the configuration of the latter bank section is shown in Figure 2. For all water depth cases as listed in Table 3, the banks on the positive side are surface-piercing.

Matrix of test conditions A subset of the KVLCC2 model test programme for bank effects executed at FHR is used as reference for the CFD computations: i.e. test results for three lateral positions at a depth of 35% UKC and for the right-most position, three UKC values (see Table 4). Only that part of the data where the vertical wall and $1/4$ slope are present, is used in this paper. Negative values for the lateral positions mean that the ship is positioned towards the vertical wall. For each case, two data sets are available: (a) one with turning propeller and (b) one with stopped propeller. The numbering in Table 4 is used in the rest of this paper to present data of each of the tests or computations. The model speed during the experiments was $0.356\,\mathrm{m\,s^{-1}}$. With a reference length of $L_{pp} = 4.2667\,\mathrm{m}$ and an average water temperature of $18.22\,^{\circ}\mathrm{C}$, this results in a Froude number of $Fr = 0.055$ and a Reynolds number of $Re = 1.448 \times 10^6$.

Presentation of the results In this study, ship-fixed forces and moments are presented. The longitudinal force X is directed forward, the transverse force Y is directed to starboard (i.e. positive when directed to the vertical wall), the heeling moment K is positive when pushing starboard into the water and the yaw moment N is positive when pushing the bow to starboard (i.e. towards the vertical wall). Both the forces and moments measured during the towing tank tests and the computed forces and moments are presented as dimensional model scale values.

Pressure and shear stress distributions are non-dimensionalised by $\frac{1}{2}\rho V_\infty^2$ and non-dimensional axial velocity distributions are obtained by dividing the axial velocity by the undisturbed velocity V_∞. Furthermore, the longitudinal vorticity component ω_x is made non-dimensional by L_{pp}/V_∞ and turbulent kinetic energy is divided by V_∞^2.

[1] `http://www.simman2014.dk`

Table 1: Main dimensions of towing tank at FHR

Total length	87.5 m
Effective length	68.0 m
Width	7.0 m
Maximum water depth	0.5 m
Length of ship models	3.5 to 4.5 m

Table 2: Hydrostatic particulars of KVLCC2 (model scale) for the bank effects test program

Parameter	unit	T0Z01(B03,B04,B05)
Length (L_{pp})	m	4.2667
Draft Amidships (T_m)	m	$0.2776 \pm 0.5 \cdot 10^{-3}$
Longitudinal CoG (X_G)	m	0.1449 ± 0.002
Vertical CoG (KG)	m	0.2776 ± 0.0008
Displacement	m^3	$0.7410 \pm 2.37e-4$
Block coefficient	–	0.8098
Mass	kg	736.2 ± 0.2
I_{XX}	kg m^2	41.0 ± 1.2
I_{YY}	kg m^2	797.3 ± 2.6
I_{ZZ}	kg m^2	831.5 ± 2.2

Table 3: Tested water depths, UKC values and test sequences

Water depth	UKC	Test sequence
0.4160 m	50%	T0Z01B03
0.3744 m	35%	T0Z01B04
0.3051 m	10%	T0Z01B06

Figure 1: Overview of towing tank with banks

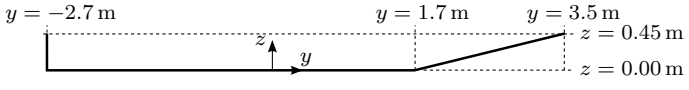

Figure 2: Cross section of the tank geometry with vertical wall and slope

Table 4: Test conditions as a function of lateral position, under keel clearance (UKC) and water depth. Cases indicated with "a" are with propulsion, "b" cases without propulsion

	$-2.1825\,\mathrm{m}$	$-2.1134\,\mathrm{m}$	$-1.7269\,\mathrm{m}$
50% UKC			case 4 (a,b)
35% UKC	case 1 (a,b)	case 2 (a,b)	case 3 (a,b)
10% UKC			case 5 (a,b)

Analysis of experimental data

For each test case, only one experiment was executed. Hence, it is not possible to compute standard deviations for the measured values as would be the case when each experiment was repeated multiple times. To judge the steadiness of the experimental data, both the normalised cumulative moving average (nCMA) and the normalised cumulative standard deviation (nCSTD) are computed. If the derivatives of these values (dnCMA and dnCSTD, respectively) approach zero, the experimental time series converges to a steady state. In addition, the Fast Fourier Transform (FFT) of the experimental time series is computed to get an idea of the frequency content of the fluctuations.

As an example, for case 4a the experimental data for X is shown in Figure 3. The top figure shows the measured force for the complete duration of the experiment in grey and in light blue ($\approx 150-200\,\mathrm{s}$) the actual data that corresponds to the part during which the model is located in the bank section with the vertical wall. This part of the time trace is used to compute the average values. Below this graph, the plots labelled *nCMA* and *nCSTD* show the normalised cumulative moving average and the normalised standard deviation for the light blue part. Both graphs approach one. On the third row, the plots show the numerically computed first derivatives of the figures in the second row on a logarithmic scale. These plots clearly show that both the mean and the standard deviation convergence as their derivatives approach zero. On row four, the FFT of the experimental data is shown. The frequency with the highest power is located at $3\,Hz$. The lowest frequency has a value that is at least an order of magnitude smaller, which indicates that the time signal does not contain a (linear) trend.

For the same test case, the sinkage at the midship location (halfway between the aft and fore perpendicular) shows a different trend (Figure 4). Until 190 seconds the convergence of the sinkage is very good, with differences of nCMA smaller than 1%. At this point, the sinkage starts to decrease with an almost linear trend until the end of the experimental data. This is reflected in the nCMA and nCSTD plots and their derivatives. The FFT plot on the lowest row shows that the lowest frequency signal has the highest power, which is an indication for a trend in the data. However, the measured difference in the sinkage between $t = 190\,\mathrm{s}$ and $t = 200\,\mathrm{s}$ is less than $0.1\,\mathrm{mm}$, which is on the same order as the accuracy of the device used for the measurement of the sinkage (Delefortrie 2015).

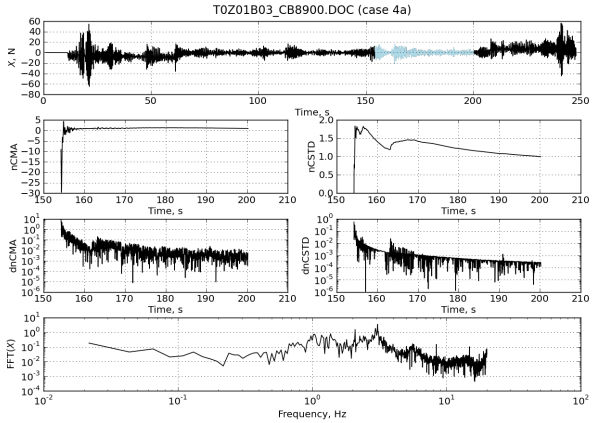

Figure 3: Convergence analysis of X for case 4a

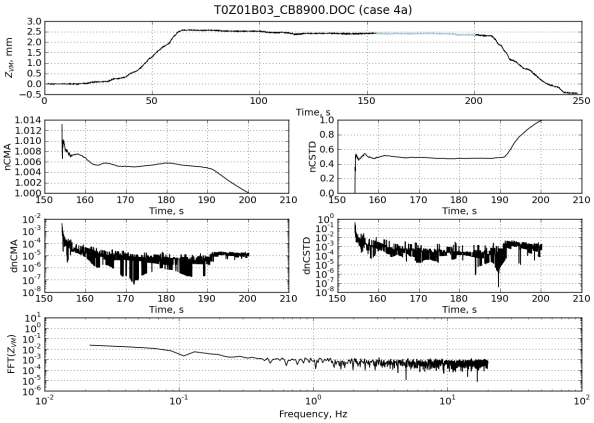

Figure 4: Convergence analysis of midship sinkage for case 4a

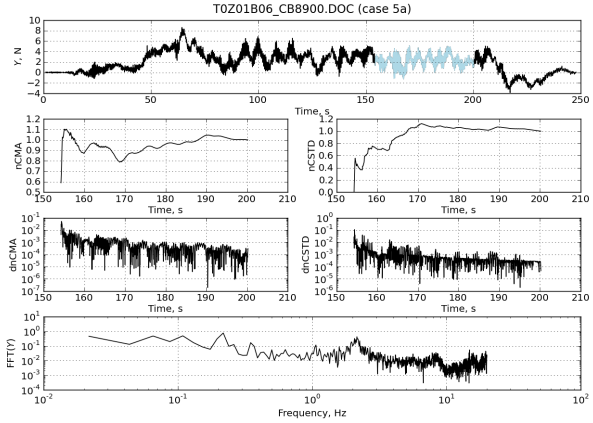

Figure 5: Convergence analysis of lateral force Y for case 5a

Table 5: Average values obtained from the measurements

Cases 1a-5a (with propulsion)

	1a	2a	3a	4a	5a
X, N	-2.024	-1.274	-0.5301	-0.2880	-1.757
Y, N	8.147	8.500	3.584	3.235	2.244
K, Nm	0.4855	0.4651	0.2106	0.09356	0.3851
N, Nm	-2.3680	-3.616	-1.332	-1.078	-4.800
T, N	2.414	2.492	2.251	2.361	2.592
Q, Nmm	39.68	47.02	42.28	44.28	46.20
Sinkage, mm	3.620	3.558	2.783	2.397	3.977
Trim, deg	-0.03759	-0.03459	-0.03180	-0.02849	-0.04049

Cases 1b-5b (without propulsion)

	1b	2b	3b	4b	5b
X, N	-3.791	-3.470	-2.508	-2.426	-3.681
Y, N	6.013	4.758	2.280	1.925	0.7887
K, Nm	0.5847	0.2757	0.1405	0.1226	0.4012
N, Nm	-0.9362	-0.9304	-0.9258	-0.3376	-5.183
Sinkage, mm	3.356	3.229	2.738	2.201	3.714
Trim, deg	-0.04302	-0.03945	-0.03449	-0.03136	-0.04521

Case 5a (10% UKC) shows significant fluctuations in the lateral force Y, as shown in Figure 5. Despite this, the derivatives of nCMA and nCSTD indicate that the time signal of the lateral force Y converges both in frequency and value. For this case, the dominant frequency is slightly larger than $0.2\,\mathrm{Hz}$, which corresponds to the low-frequency fluctuations that are visible in the time plot.

Average values

Data averages are computed with a subset of the full test, the first 27% and the last 10% of the data is not used in the averaging process, the resulting interval from 27% to 90% corresponds to the light-blue part of the time plots as displayed in Figs. 3, 4 and 5. The average values obtained from the experiments are presented in Table 5. Note that for the cases without propulsion, thrust and torque values are not shown, although these values were measured as well. All values are rounded to four significant digits.

Water surface elevation

Data from multiple wave gauges were recorded during the experiments. One of these gauges is located halfway between the beginning and the end of the bank configuration, between the vertical wall and the ship, at a longitudinal position of $x_{wg} = 19\,\mathrm{m}$. Its lateral position in the tank is $y_{wg} = -2.68\,\mathrm{m}$. Hence, there is a gap of two centimetres between the vertical wall and the wave measurement device, as the vertical wall is located at $y = -2.7\,\mathrm{m}$ (as shown in Figure 2). For methods where the free surface is taken into account, these water surface elevation measurements can be used to validate the free surface position. Conversion of the position of the wave gauge to a ship-fixed coordinate system is done as follows:

$$x_{wg,rel} = \frac{x_{ship} - x_{wg}}{L_{pp}} \tag{1}$$

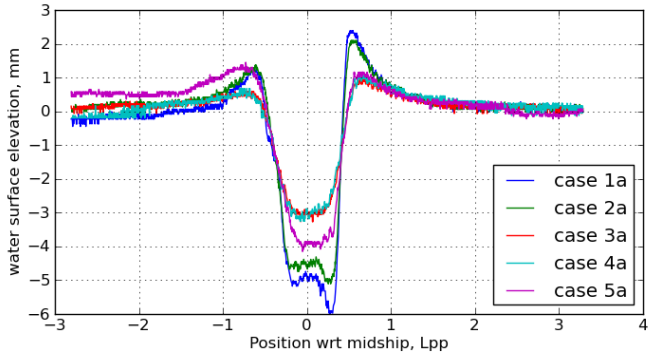

(a) With propulsion

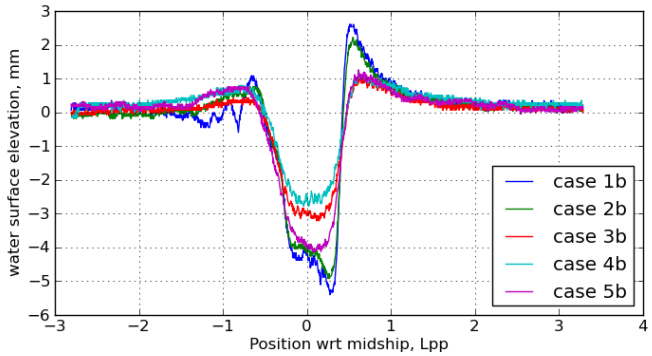

(b) Without propulsion

Figure 6: Measured wave elevations at wave gauge 5

where x_{ship} is the longitudinal position of the midship location in the towing tank coordinate system, x_{wg} is the longitudinal position of the wave gauge in the towing tank coordinate system and $L_{pp} = 4.2667\,\mathrm{m}$ is the ship model length between perpendiculars. The converted wave measurements are shown in Figure 6 for the cases with and without propulsion. Sign conventions are such that positive x-coordinates correspond to positions ahead of the midship location, and positive y-coordinates correspond to an increase in water surface height.

For all cases, an upward peak is observed when the ship bow passes the wave gauge. The peak value is inversely proportional to the lateral distance to the quay; for cases 3, 4 and 5 the peak value is the same. Between the ship and the quay, the depression is more pronounced as the ship sails closer to the quay, but here, also the UKC value has an influence on the maximum depression. For cases 1 and 2 (both a and b), the depression is not symmetric with respect to the ship length, but shows a peak near $L_{pp}/4$ ahead of the midship location. Case 5a is the only one for which the peak in water surface elevation near the aft perpendicular is higher than the peak at the bow.

COMPUTATIONAL SETUP

MARIN

REFRESCO is a viscous-flow CFD code that solves multi-phase (unsteady) incompressible flows with the RANS equations, complemented with turbulence closure models, cavitation models and volume-fraction transport equations for different phases, see Vaz et al. (2009). The equations are discretised using a finite-volume approach with cell-centred collocated variables and in strong-conservation form. A pressure-correction equation based on the SIMPLE algorithm is used to ensure mass conservation as discussed by Klaij and Vuik (2013). Time integration is performed implicitly with first or second-order backward schemes. At each implicit time step, the non-linear system of velocity and pressure is linearised with Picard's method and either a segregated or coupled approach is used. In the latter, the coupled linear system is solved with a matrix-free Krylov subspace method using a SIMPLE-type preconditioner (Klaij and Vuik 2013). A segregated approach is always adopted for the solution of all other transport equations. The implementation is face-based, permitting grids with elements consisting of an arbitrary number of faces (hexahedra, tetrahedra, prisms, pyramids, etc.), and, if needed, h-refinement i.e. hanging nodes. State-of-the-art CFD features such as moving, sliding and deforming grids, as well automatic grid refinement are also available in the code.

For turbulence modelling, RANS/URANS, Scale Adaptive Simulation (SAS) (Menter and Egorov 2005), ((I)D)DES, Partially Averaged Navier Stokes (PANS) and LES approaches are available, see Pereira et al. (2014). The Spalart correction (proposed by Dacles-Mariani et al. 1995) to limit the production of turbulence kinetic energy based on the stream-wise vorticity can be activated. Automatic wall functions are available.

The code is parallelised using MPI and sub-domain decomposition, and runs on Linux workstations and HPC clusters. REFRESCO is currently being developed, verified and validated at MARIN in the Netherlands in collaboration with IST (Lisbon, Portugal), USP-TPN (University of São Paulo, Brazil), Delft University of Technology, the University of Groningen, the University of Southampton, the University of Twente and recently Chalmers University of Technology.

REFRESCO *computational domain and setup* Due to the different water depths and distances of the ship to the vertical wall, new grids had to be made for each case. Free surface deformation was not taken into account in the REFRESCO computations. To account for the dynamic trim and sinkage the experimental values were applied in the grid generation. This means that also for the cases with and without propulsion, separate grids had to be generated. To ensure grid similarity between the cases and between different grid densities, the meshing process was automated using scripts. Unstructured grids with hexahedral elements were generated using HEXPRESS. At the hull and rudder surfaces, an inflation layer was added to be able to capture the high gradients in the boundary layer.

The inlet and outlet boundaries were located at $4L_{pp}$ forward and $4L_{pp}$ aft of the aft perpendicular of the ship. In Figure 7 the domain and boundary definitions are shown. Symmetry boundary conditions were applied on the undisturbed water surface (top). On the hull and rudder surface, no-slip and impermeability

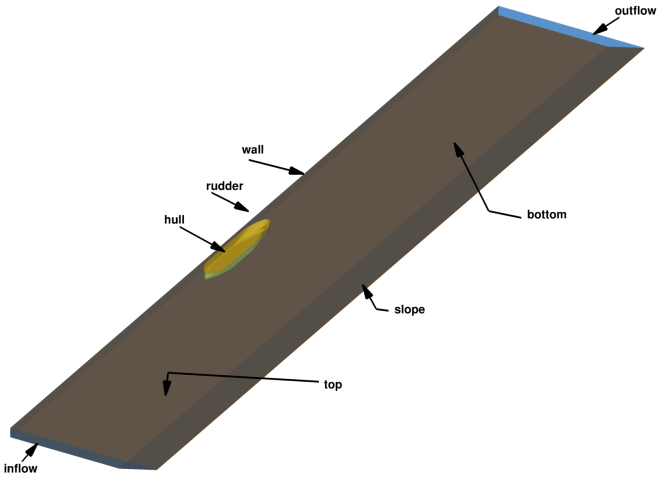

Figure 7: Domain for REFRESCO computations

Table 6: Grid densities for REFRESCO grid sensitivity study, case 1b

Grid Id	Number of cells n_c	Faces on hull surface	y^+_{max} on hull surface
Coarse	2 922 462	31 750	0.51
Medium	4 523 429	45 467	0.46
Fine	7 449 527	68 385	0.34
Very fine	11 453 879	96 743	0.33
Extremely fine	26 174 442	183 077	0.25
Ultimately fine	34 731 429	228 742	0.23

boundary conditions are used ($\overline{u} = 0$). Due to the application of the inflation layer at these surfaces, the y^+_{max} values are around 0.5 and therefore the boundary layer is resolved down to the wall. On the vertical wall, on the slope and on the bottom surface, the boundary condition is set to moving wall/fixed slip ($\overline{u} = \overline{V_\infty}$ with V_∞ the inflow velocity). At these boundaries wall functions are used to avoid large grid densities. A pressure boundary condition is applied at the outflow and inflow boundary conditions at the inflow. The inflow turbulence intensity is set to 1% and the eddy viscosity at the inflow to $\mu_t = 1\mu$. All calculations were conducted for a Reynolds number $Re = 1.5 \times 10^6$. The calculations presented in this study were all conducted without incorporating free-surface deformation and assuming steady flow. The $k - \omega$ SST model (Menter et al. 2003) was used as turbulence closure. For the *a* cases, the propeller action was achieved by coupling REFRESCO with the potential flow code PROCAL (Vaz and Bosschers 2006) and using the obtained forces on the propeller as body forces in the viscous-flow computation, see e.g. Rijpkema et al. (2013). In each propelled case, the propeller rate of revolutions was set to $345.3\,\mathrm{min}^{-1}$ and the propeller thrust was obtained from the computation. For the *b* cases, the stopped propeller was not considered in the computations.

REFRESCO *solution verification* To obtain information about the sensitivity of the solutions to the grid density, a series of grids with various densities was generated for case 1b. Each grid was made using identical levels of refinements. The grid density was controlled by adjusting the number of cells in the initial base mesh. To maximise the grid similarity between different grid densities, the refinement diffusion was increased when increasing the grid density. For the hull and rudder surface, the first cell height was adjusted as a function of the density as well. Unfortunately, the way in which HEXPRESS generates the inflation layer does not allow users to fully control the mesh similarity close to walls. This means that upon grid refinement, the inflation layer becomes thinner and eventually, extrapolation to an infinitely fine grid would result in a solution on a grid without inflation layer. Therefore, a formal uncertainty estimate based on geometrically similar grids cannot be made. The study presented should therefore be considered as a grid sensitivity study. The grid sizes that were investigated are shown in Table 6.

For the finest grid (*ultimately fine*), the iterative convergence for case 1b is shown at the top of Figure 8. The convergence shows a clear oscillation of the forces (standard deviation of 1.6% in X and 6.6% in Y) and moments (standard deviation of 4.0% in K and $0.3\,\mathrm{Nm}$ in N, which is larger than the mean value) and the uncertainty in the solution due to the iterative process can therefore not be neglected. This means that the discretisation error will be contaminated by scatter due to insufficient iterative convergence, see Eça and Hoekstra (2009). All computations have been conducted assuming steady flow, but the oscillatory behaviour of the global quantities during the iterative process in each case indicates that unsteady effects may be present in the flow and an unsteady solution approach may be more appropriate. In the remainder of this paper, the forces and moments shown will be based on an average of the last part of the convergence history for each case.

In the bottom graph of Figure 8, the integral results for case 1b for the various grid densities are shown. On the horizontal axis, the relative step size $h_i/h_1 = \sqrt[3]{n_{c,1}/n_{c,i}}$ is shown. A relative step size of 1 represents the result for the finest grid, while higher step sizes correspond to coarser grid results. A formal uncertainty estimate (e.g. following Eça and Hoekstra (2014)) could not be made due to apparent divergence of the results upon grid refinement, leading to unrealistically high uncertainty estimates. From the results, it can be concluded that even for the finest grids the solution still changes and even finer grids should be used in order to avoid too large uncertainties in the results due to discretisation errors. This conclusion confirms the observations by L. Zou and Larsson (2013) in which also large uncertainties were found for bank-effects computations.

In the graphs presented in this paper regarding the trends of bank suction effects, REFRESCO results for the *medium* grid are included. Based on the solution verification, it is found that the numerical uncertainty in the results is rather large and therefore it will be hard to draw quantitative conclusions on the accuracy of the modelling approach. Any deviations from the true value can be caused by either modelling errors, or due to uncertainties in the solutions. In future studies, finer grids and probably an unsteady solution approach should be adopted to better quantify the

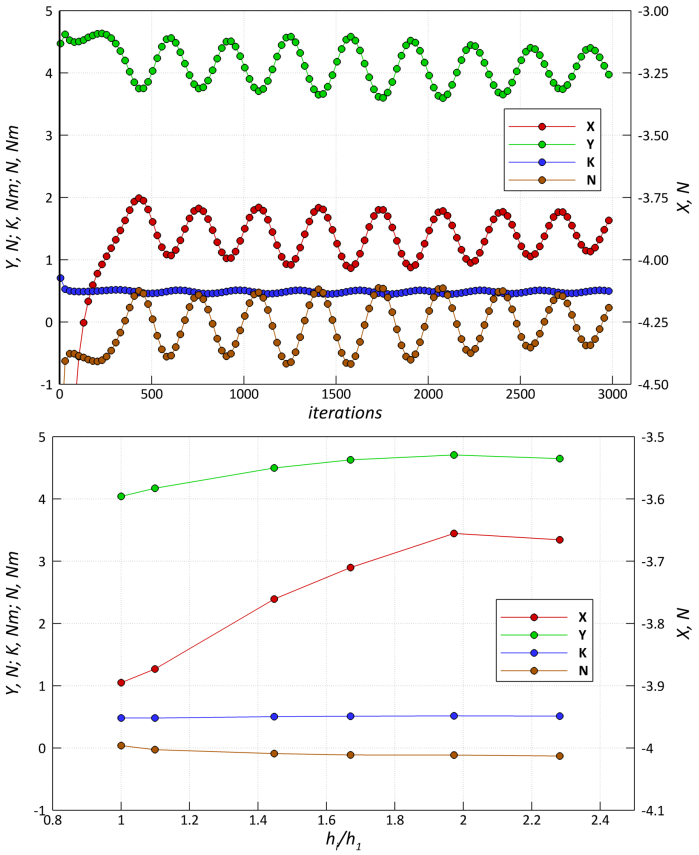

Figure 8: Case 1b: solution verification for REFRESCO. top: iterative convergence, bottom: grid sensitivity

trends.

ROPES has been developed for the prediction of ship-ship interaction forces in shallow water of arbitrary depth. The computational method used in ROPES is based on three-dimensional potential flow and the double-body assumption. This means that free-surface effects of vessels are not accounted for. Furthermore, trailing wakes are not used in ROPES, so the potential flow model does not include lift effects. The flow equations are solved using standard zero-order panels and Rankine sources with or without the effect of restricted water depth and channel walls (Korsmeyer et al. 1993; Pinkster 2004). Based on the solution of the source strengths on the panels describing the various bodies, the hydrodynamic forces on the ships are computed based on equations developed by Xiang and Faltinsen (2010). These equations are used to compute the complete set of hydrodynamic forces on all bodies. ROPES is applicable to multi-body simulation scenarios involving various ships and port structures.

A close up view of the panel distribution on the hull and on a part of the vertical wall is given in Figure 9. The vertical wall extends from $x/L_{pp} = -4$ to $x/L_{pp} = 4$. The hull is represented using 2438 panels, while 2184 panels are used to describe the vertical and sloped wall. Since ROPES cannot handle lifting surfaces, the rudder has been removed from the ship geometry. The com-

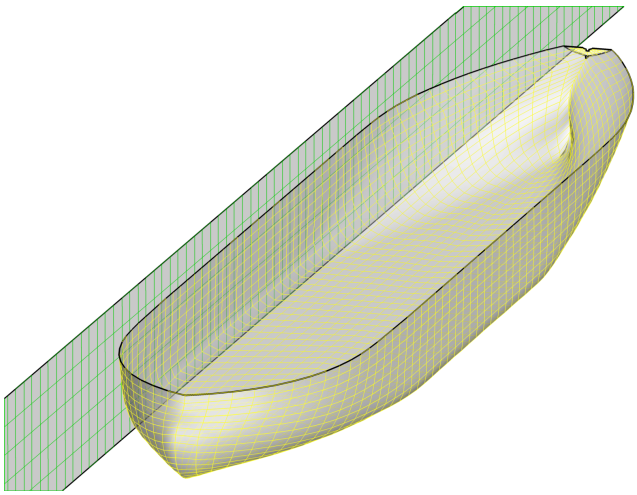

Figure 9: Panel distribution on hull and part of the vertical wall for ROPES computations

putations were executed at full scale conditions and the resulting forces and moments were converted to model scale.

FHR

ISIS-CFD The ISIS-CFD solver that is available as a part of the FINE/Marine CFD computing suite, is an incompressible, unsteady, Reynolds-averaged Navier-Stokes (URANS) solver mainly devoted to marine hydrodynamics. The solver features several sophisticated turbulence closure models: apart from the classical two-equation $k-\epsilon$ and $k-\omega$ models, the anisotropic two-equation Explicit Algebraic Stress Model (EASM), as well as Reynolds Stress Transport Models, are available with or without rotation corrections (Deng and Visonneau 1999). All turbulence models are compatible with wall-function or low-Reynolds near wall formulations. Hybrid LES turbulence models based on Detached Eddy Simulation (DES) are also implemented and are validated on automotive flows characterised by large separations (Guilmineau et al. 2013). Additionally, several cavitation models are available in the code.

The solver is based on the finite volume method to build the spatial discretisation of the transport equations. The unstructured discretisation is face-based. While all unknown state variables are cell-centred, the systems of equations used in the implicit time stepping procedure are constructed face by face. Fluxes are computed in a loop over the faces and the contribution of each face is then added to the two cells next to the face. This technique poses no specific requirements on the topology of the cells. Therefore, the grids can be completely unstructured: cells with an arbitrary number of arbitrarily-shaped faces are accepted. Pressure-velocity coupling is enforced through a Rhie & Chow SIMPLE type method: at each time step, the velocity updates come from the momentum equations and the pressure is given by the mass conservation law, transformed into a pressure equation. In the case of turbulent flows, transport equations for the variables in the turbulence model are added to the discretisation. Free-surface flow is simulated with a multi-phase flow ap-

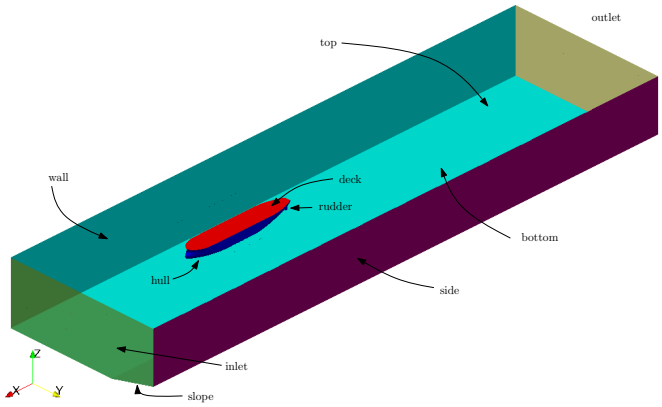

Figure 10: Domain for ISIS-CFD computations

proach: the water surface is captured with a conservation equation for the volume fraction of water, discretised with specific compressive discretisation schemes (Queutey and Visonneau 2007). The technique included for the 6 degrees of freedom simulation of ship motion is described by Leroyer and Visonneau (2005). Time-integration of Newton's law for the ship motion is combined with analytical weighted or elastic analogy grid deformation to adapt the fluid mesh to the moving ship. To enable relative motion of appendages, propellers or bodies without having recourse to overlapping grids, a sliding grid approach has been implemented. Propellers can be modelled using actuator disc theory, by coupling with boundary element codes (RANS BEM coupling, see Deng et al. 2013), or direct discretisation through e.g. rotating frame method or sliding interface approaches. Finally, a anisotropic automatic grid refinement procedure has been developed which is controlled by various flow-related criteria (Wackers et al. 2014).

Parallelisation is based on domain decomposition. The grid is divided into different partitions; these partitions contain the cells. The faces on the boundaries between the partitions are shared between the partitions; information on these faces is exchanged with the MPI (Message Passing Interface) protocol. This method works with the sliding grid approach and the different subdomains can be distributed arbitrarily over the processors without any loss of generality. Moreover, the automatic grid refinement procedure is fully parallelised with a dynamic load balancing working transparently with or without sliding grids.

Computational domain and setup The lateral cross section of the domain is the same as the geometry shown in Figure 2. The top of the domain is located $0.5L_{pp}$ above the water surface. At this surface, the pressure is prescribed using the *Updated hydrostatic pressure* boundary condition of ISIS-CFD. The inlet is located $1.5L_{oa}$ ahead of the bow of the ship, and the outlet is located $2.5L_{oa}$ aft of the stern, hence the total domain length is approximately $5L_{oa}$. For both of these surfaces, a far-field boundary condition is applied ($V = V_\infty$). The bottom and the surface-piercing tank walls are modelled as solid walls having a relative velocity with respect to the ship. Wall function boundary conditions are applied at these surfaces. A no-slip condition is applied at the rudder surfaces and the hull except for the deck, where a slip condition is applied. The lateral wall on port side has a slip condition as well. No wall functions are used on the the hull and rudder surfaces, i.e. the flow is resolved down to the wall ($y^+_{max} \approx 0.5$).

Table 7: Grid sizes for the computations of FHR

Case Id	Number of cells n_c
case 1a,b	16 077 704
case 2a,b	16 029 616
case 3a,b	16 066 391
case 4a,b	15 966 300
case 5a,b	15 845 064

Propulsion is modelled using an actuator disk, for which the measured thrust and torque values are used as input (see Table 5). This method requires extra grid refinements near the propeller location. The same grids are used for the propulsive cases and the non-propulsive cases, hence five meshes were generated. For each combination of lateral position and water depth, first a computation without propulsion is executed after which the propulsive cases are computed using the solution of the non-propulsive case as initial condition.

Trim and sinkage are solved for in the ISIS-CFD computations. To ensure that due to sinkage, the cells below the hull are not compressed too much (which may result in negative cell volumes), the hull is meshed three millimetres below the hydrostatic position. Vertically, the centre of gravity is located on the waterline. Longitudinally, it is located $0.1482\,\mathrm{m}$ ahead of the midship location. This value is approximately 2 millimetre aft of the longitudinal location of the centre of gravity as recorded in the experiments (see Table 2).

For each case the grid contains approximately 16 million cells, the actual numbers are documented in Table 7.

Initially, all computations were run using a first-order time discretization scheme that uses a quasi-static approach to update the attitude and position of the ship such that the resulting accelerations approach zero. For three cases (1b, 2b & 3b), a second-order time discretization scheme – where Newton's laws are tightly coupled to the flow motion at each time step – has been used as well[2]. For these cases, the inertia moments for the ship hull are required as input. In the analyses that follow, the ISIS-CFD computations using a first-order time discretization are labeled *ISIS-CFD*, whereas the computations that use a second-order time discretization are labeled *ISIS-CFD unsteady*.

Solution verification For case 3b, derived grids were generated for solution verification. The cell sizes were modified by adjusting the cells sizes in the initial Cartesian grid. For example, the

[2]Due to time constraints, not all cases could be run in this mode.

Table 8: Grid densities for ISIS-CFD grid sensitivity study, case 3b

Grid Id	Number of cells n_c	Faces on hull surface	y^+_{max} on hull surface
Very coarse	4 966 527	123 845	0.79
Coarse	9 091 550	236 799	0.69
Medium	16 066 391	411 298	0.54
Fine	29 780 394	771 173	0.40

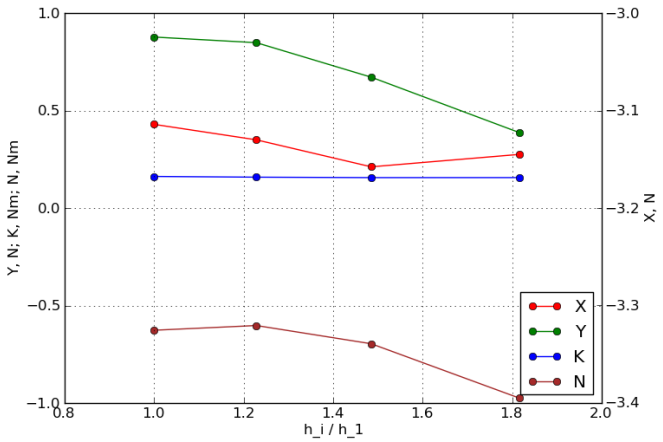

Figure 11: Grid densities for ISIS-CFD computations, case 3b

fine mesh was generated by decreasing the linear dimensions of the initial cells by a factor 1.4. Furthermore, for refinement surfaces and refinement boxes with absolute target cell sizes (such as the surfaces used for water surface refinement), the target cell size values were modified by the inverse of this refinement factor. For the hull and rudder, the first cell size was adjusted as well, resulting in lower y^+ values for the finer meshes (as shown in Table 8).

The values of the integral quantities for the four grids are shown in Figure 11. Similar to the solution verification of REFRESCO (see above), the horizontal axis of this figure shows the relative step size $h_i/h_1 = \sqrt[3]{n_{c,1}/n_{c,i}}$: the finest grid has a relative step size of one. These results show that although the computed integral quantities show converging trends, the *medium* grid sizes used in the rest of this paper may not be refined enough for sufficiently small uncertainties due to discretisation errors.

Adaptive grid refinement For case 3b, ECN/CNRS performed a computation using ISIS-CFD with adaptive grid refinement (AGR) starting from a steady solution obtained on a coarse mesh (approximately 5M cells) that was provided by FHR. A new combined refinement criteria for both the free-surface and the vortical structures has been used (Wackers et al. 2015). The minimum size limit for refined cells has been retained to $0.002\,\mathrm{m}$ and is activated each 50 steps of the time marching procedure similar to FHR in order to find a steady solution. This leads to a refined grid of about 20M cells.

Overview of computational settings

For the five test cases without propulsion, results from L. Zou et al. 2011 will be included in the comparison between CFD predictions and the experiments. A summary of the settings for the computations used in the force and flow field comparisons as discussed later in this paper is given in Table 9.

COMPARISON OF GLOBAL FORCES AND MOMENTS

The computed global forces and moments will be compared with the experimental data both on an absolute and relative scale. For the absolute comparisons, the dimensional values are used as-is. For relative comparisons, the experimental results are used as a reference and for each CFD result, the relative comparison error is computed as follows,

$$E(\%D) = \frac{S - D}{D} \times 100, \tag{2}$$

where S is the numerical result and D the experimental reference value.

The integral quantities that are compared are the resultant longitudinal force X acting on the hull and rudder, the lateral force Y, the roll moment K and the yawing moment N. For the X-axis of plots, the lateral position of the ship in the tank (case 1, 2 and 3) and under keel clearance (case 3, 4 and 5) is used. Hence, two sets of plots are created with the third case appearing in both. For all of these, separate plots will be made for the a and b cases (with and without propulsion, respectively). Afterwards, the computed thrust values will be compared with the experimental data. In all figures that show absolute values, the case names are shown above the plot area.

Forces and moment comparison

Qualitatively speaking, the CFD results are able to capture the trends that are present in the EFD results. Both CFD codes predict the trends in the forces and moments as a function of the distance to the bank and the under keel clearance. For example, REFRESCO and ISIS-CFD predict that as the ship approaches the bank, the drag on the hull and the bank attraction force increase. The differences between the roll moments (K) and yawing moments (N) are small between the two CFD codes.

Quantitatively, large differences can be seen, especially for the more extreme conditions, i.e. close to the vertical wall, or with small under-keel clearance. For example, REFRESCO and ISIS-CFD predict for the 10% UKC case that the lateral force Y acts repulsive, whereas the EFD results show that for all water depths the lateral forces attracts the ship to the wall. Unfortunately, uncertainty estimates are not available for the experiments, and therefore it is not possible to conclude whether the deviations are due to modelling errors in the CFD, or due to inaccuracies in the EFD (or both). Future work on experimental uncertainties and more in-depth CFD studies for the extreme cases is highly rec-

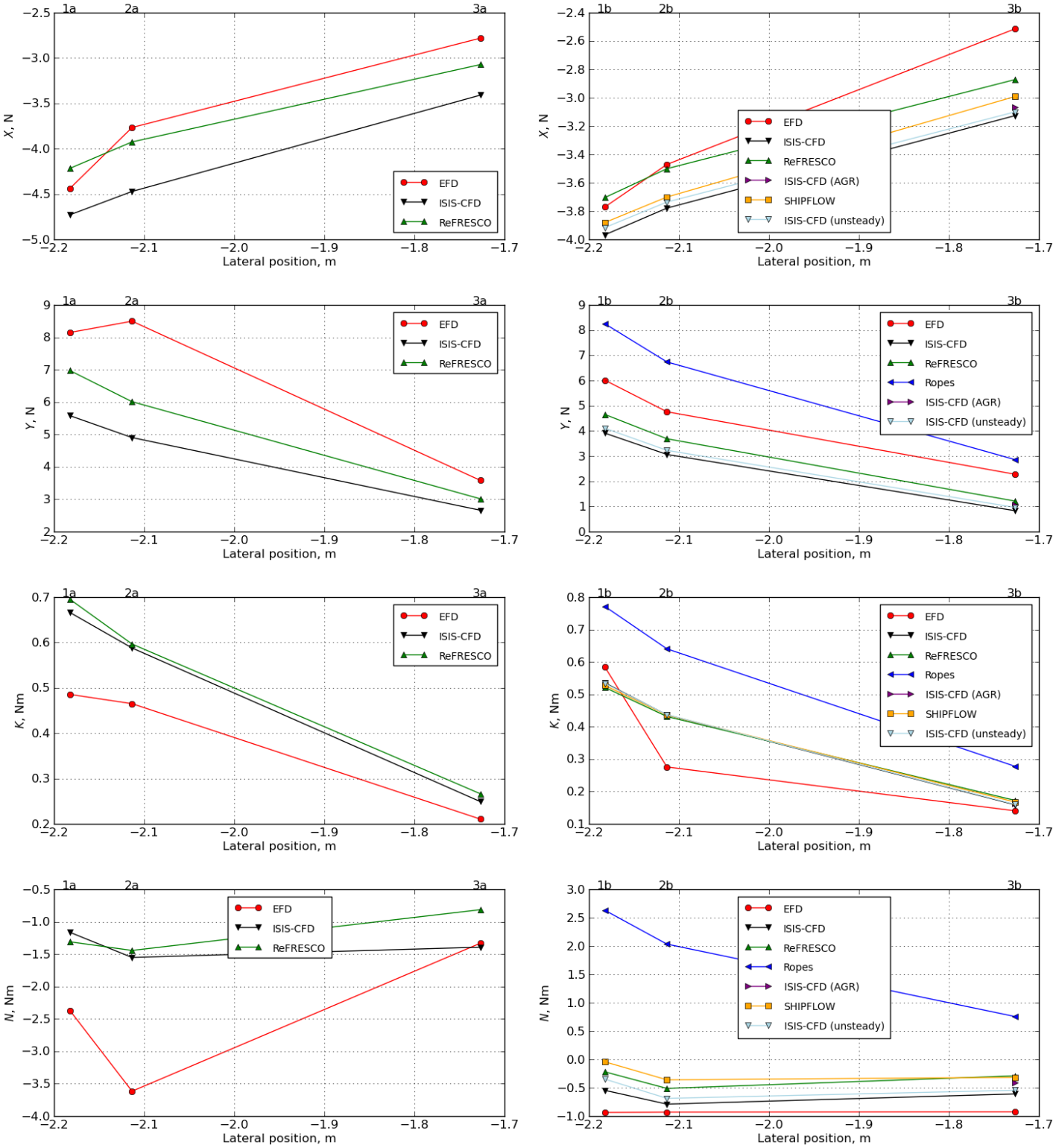

Figure 12: Resulting forces and moments as a function of lateral distance to the quay (left: with propulsion, right: without propulsion)

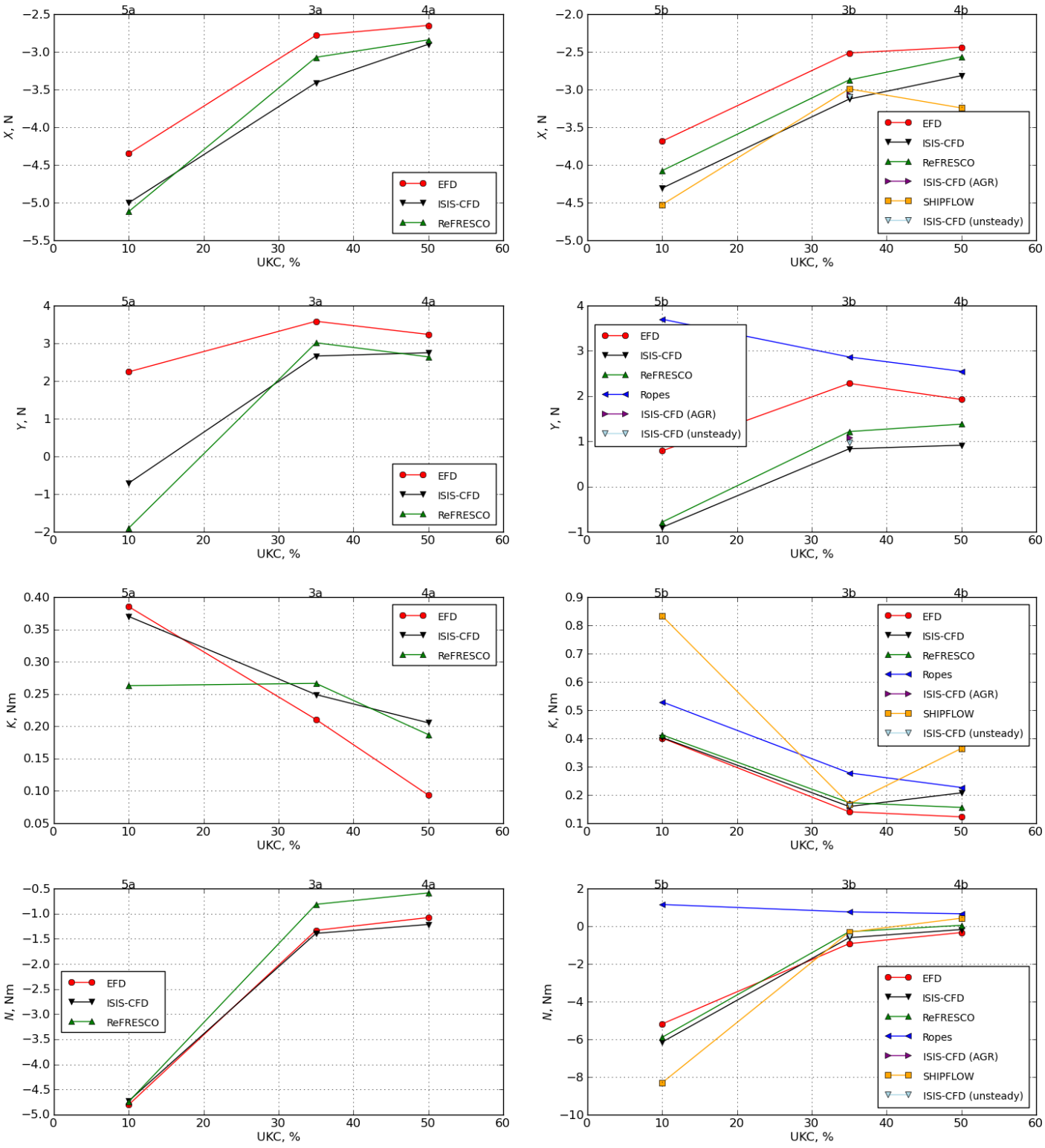

Figure 13: Resulting forces and moments as a function of under keel clearance (left: with propulsion, right: without propulsion)

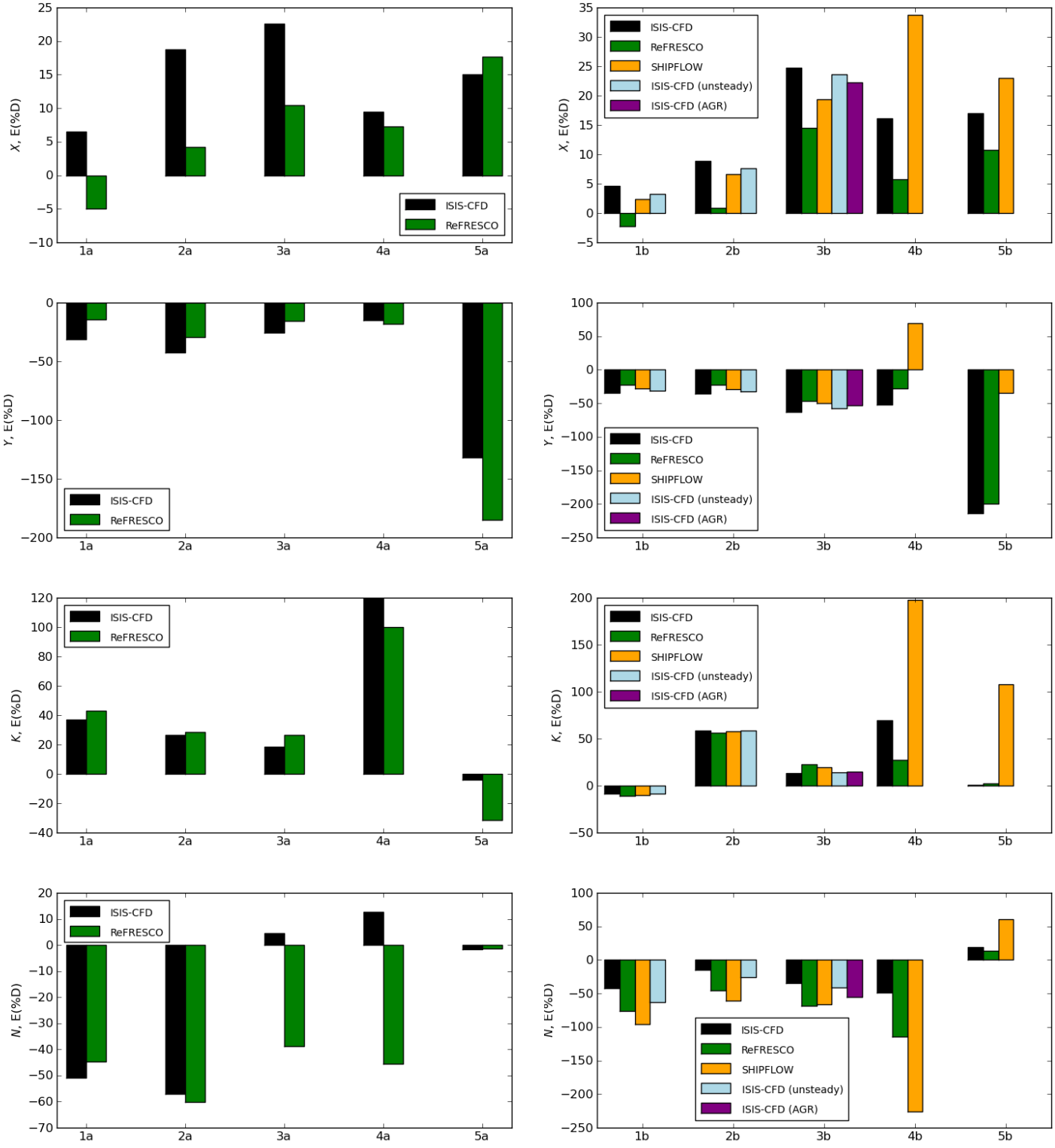

Figure 14: Relative errors of the CFD results (left: with propulsion, right: without propulsion)

Table 9: CFD computation settings

	Turbulence model	y^+	Free surface	Time discr. order	Space discr. order	Propeller (a cases)	Propeller (b cases)	Approx. mesh sizes
ISIS-CFD	EASM	<0.5	VOF	1^{st}	2^{nd}	Actuator disc	-	16×10^6 (incl. air)
ISIS-CFD (AGR)	EASM	<0.5	VOF	1^{st}	2^{nd}	-	-	20×10^6 (incl. air)
ISIS-CFD (unsteady)	EASM	<0.5	VOF	2^{nd}	2^{nd}	-	-	16×10^6 (incl. air)
REFRESCO	$k-\omega$ SST	<0.5	no	-	2^{nd}	BEM coupling	-	5×10^6
SHIPFLOW (L. Zou and Larsson 2013)	$k-\omega$ SST	<1.0	no	-	2^{nd}	-	No slip surface	2×10^6 (overset)

ommended.

The ISIS-CFD results with AGR (Figure 12 and Figure 13) show that by carefully choosing the adaptation criteria, adaptive grid refinement can give (small) improvements over methods where this is not used.

The differences between the steady and unsteady computations with ISIS-CFD for case 1b, 2b and 3b show that generally speaking, a small improvement is achieved with a second-order time discretization compared to a first-order time discretization. However, the computing time to reach a sufficiently converged solution is significantly higher for the second-order method.

ROPES predicts the wrong sign for the yawing moment (Figure 12 and Figure 13), i.e. a moment turning the bow towards the vertical wall, instead of away from the wall as predicted by the viscous-flow codes and found during the experiments. Furthermore, the force towards the bank is considerably over-predicted. More details of the difference between the potential flow results and the viscous-flow results will be discussed below. The ROPES results have been left out of the relative comparisons (Figure 14) due to the large errors in the absolute plots. In general, the REFRESCO results are closer to the experimental values than those of ISIS-CFD or SHIPFLOW, especially for X and Y. Differences between the results for the roll and yawing moment are smaller. For case 4b, the SHIPFLOW results show errors that are significantly larger than the errors for the other contributions.

Thrust comparison

In Figure 15, the thrust values obtained in the REFRESCO computations are presented together with the experimental values on an absolute scale, first as a function of the lateral position for case 1, 2 and 3 (Figure 15a), and afterwards, as a function of the under keel clearance for case 3, 4 and 5. The relative errors computed using Equation 2 are displayed for all cases in Figure 15c. On an absolute scale, the computed thrust values deviate no more than 0.5 Newton from the experimental values. For case 1a and 2a, the trust is under-predicted by approximately 15%, whereas for case 3a and 4a, it is predicted too high by about 11% and 9%, respectively. For case 5a, the error is less than 0.5%. In general, it is seen that the trend as a function of the water depth is reasonably captured, but not the trend due to the distance to the bank. In the present computations, no special treatment of the water depth or distance to the bank was done, and PROCAL has not been specifically developed for propellers operating in severely separating flow such as found in this study (see the discussion of the flow below). This may explain part of the deviations from the measurements.

COMPARISON OF LOCAL QUANTITIES

Discussion of the flow

As can be expected, the influence of the bank or bottom becomes more severe when the ship is located closer to the side wall or when the water depth reduces. In Figure 16, the limiting streamlines on the hull and the shear stress distribution on the hull and bottom are given to illustrate the flow. For all considered cases, a stagnation point is found on the bow. Depending on the closeness of the bank, the stagnation point tends to move to the starboard (bank) side, due to the displacement effect of the hull, deflecting the flow around the hull towards port side, away from the bank, in the fore ship area. This can be seen in the direction of the limiting streamlines aft of the bow. The flow accelerates between the vertical side of the ship and the side wall, resulting in a low pressure area and subsequently a suction force towards the bank. Just forward of midship, the limiting streamlines gradually change direction and show that the flow is directed towards the bank again in the aft area of the hull. Around the aft ship, the restriction of the flow due to the bottom and/or bank causes the flow to separate and reversal occurs. This is clearly seen in the diverging stream lines and low shear stress values at the starboard side of the aft ship. The separation also pushes the flow in the aft ship away from the bank again. In Figure 17, the axial velocity distributions at the propeller plane (looking aft) are given for cases 1b, 3b and 5b. In each case large areas of flow reversal are found and it is seen that these areas increase when moving closer to the wall (case 1b) or when the water depth reduces (case 5b).

Water surface elevation

For the ISIS-CFD computations, the water surface elevation was extracted along a line parallel to the quay, 0.02 metre from the quay. The longitudinal coordinate is made dimensionless using the characteristic ship length L_{pp} and an offset is applied to set the origin at the midship location. After conversion to millimetre, the results as shown in Figure 18 are obtained for the cases with and without propulsion, respectively. For case 3b, results for a computation with adaptive grid refinement (AGR) are presented as well, these are labeled *ISIS-CFD (AGR)*. For cases 1b, 2b and 3b, results of computations using a second-order time integration scheme are shown as well, these are labeled *ISIS-CFD*

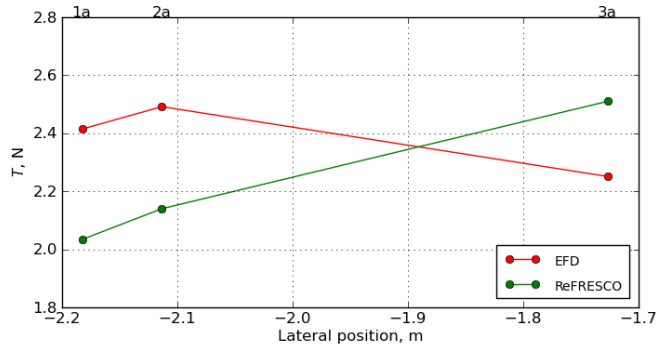

(a) T versus lateral position

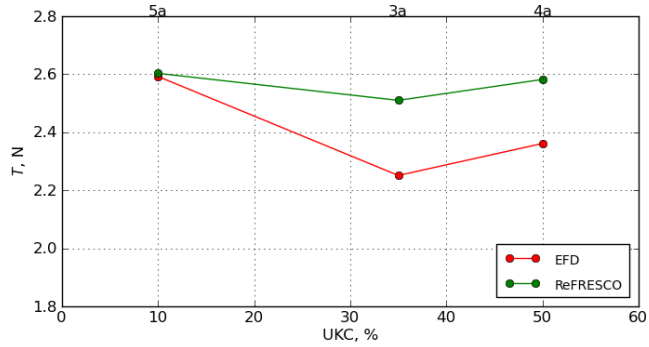

(b) T versus under keel clearance

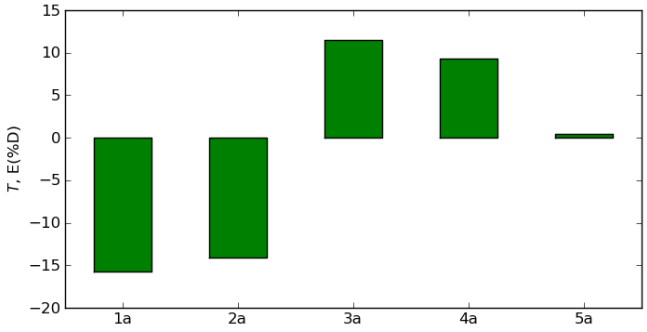

(c) Relative error of T

Figure 15: Thrust computed with the REFRESCO-PROCAL coupling, for given RPM of $345.3\,\mathrm{min}^{-1}$

(unsteady).

Except for case 1 (both a and b), all computational results predict the maximum value of the trough with an error that is one millimetre or less. For case 5b (Figure 18j), the depression at the midship location is under-predicted by 0.5 millimetre, whereas in the other cases, it is over-predicted. The asymmetry in the depression observed for cases 2a and 2b in the experimental data is predicted with the CFD results, see Figure 18c and Figure 18d. This asymmetry is also observed for cases 1a and 1b. For the latter case, the unsteady result shows that the computational result predicts the asymmetry in the shape of the depression. For cases 3 and 5, the results of FHR display an abnormal peak in water surface elevation near $x = 0.24L_{pp}$. Inspection of the free surface and grid shows that near this point, there is a change in vertical resolution of the grid near the water surface. For the steady ISIS-CFD results for cases 1a, 1b, 4b and to a lesser extend 2b and 4a, oscillations are present near the stern of the ship (between the

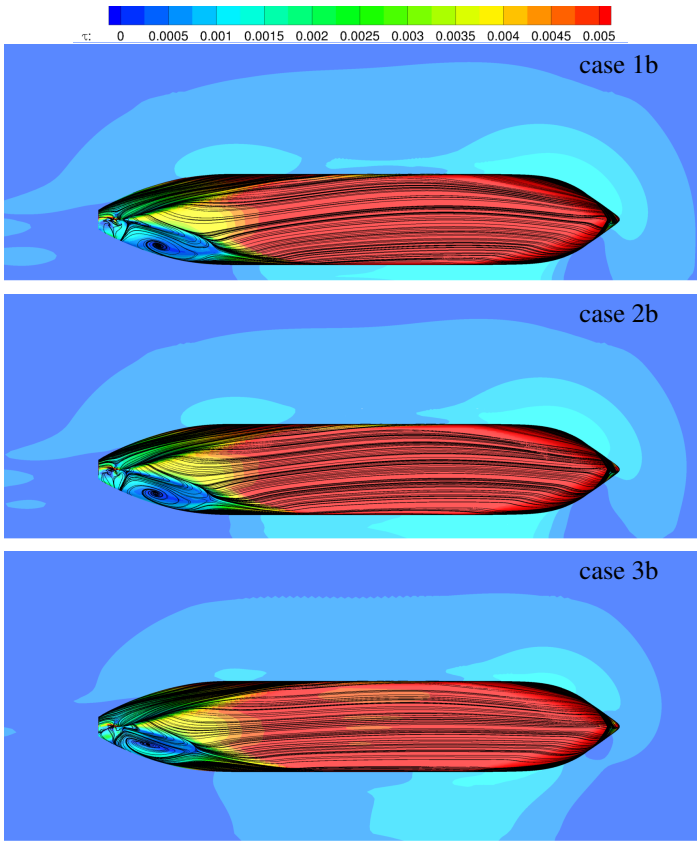

Figure 16: Hull limiting streamlines and non-dimensional shear stress as a function of distance from the vertical bank, REFRESCO

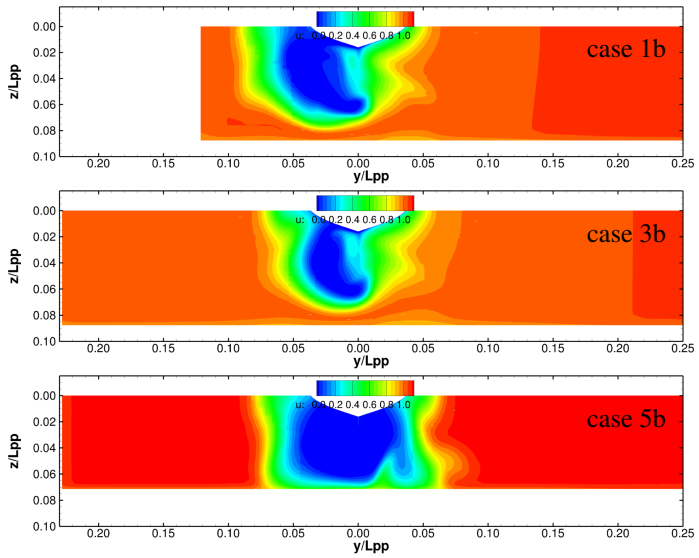

Figure 17: Axial velocity at propeller plane, REFRESCO

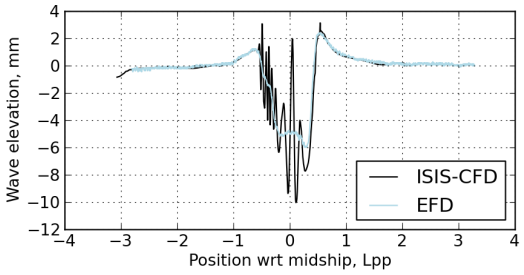

(a) Case 1a

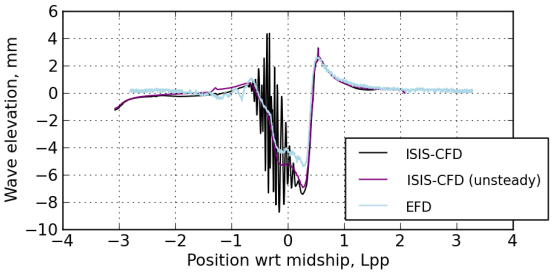

(b) Case 1b

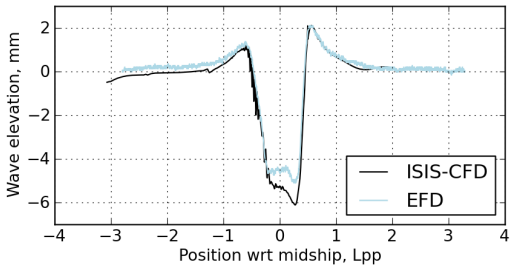

(c) Case 2a

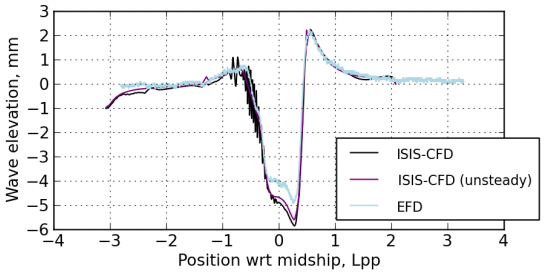

(d) Case 2b

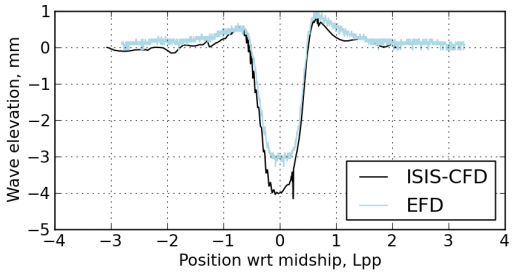

(e) Case 3a

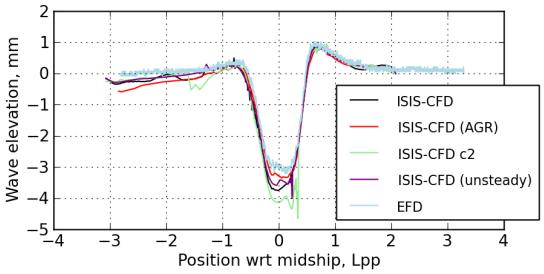

(f) Case 3b

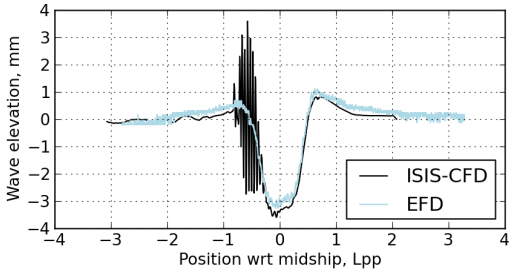

(g) Case 4a

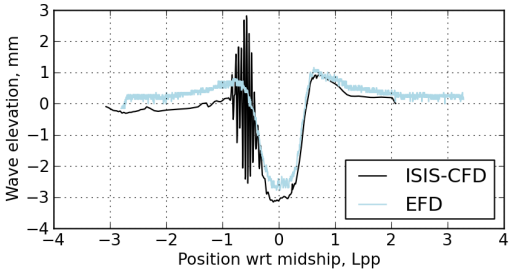

(h) Case 4b

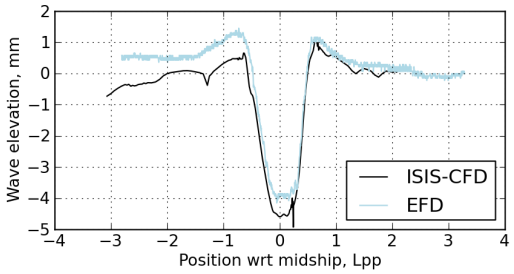

(i) Case 5a

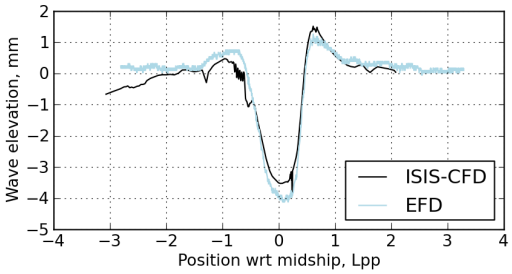

(j) Case 5b

Figure 18: Comparison of experimental and computed wave elevations (left: with propulsion, right: without propulsion)

ship and wall).

These fluctuations are not present for the AGR computation for case 3b, nor for unsteady computations of 1b, 2b and 3b. The fact that these oscillations are present for the steady computation and not for the unsteady computation is surprising, since the steady solution is obtained using a first-order scheme with more numerical damping. The absence of the oscillations in the AGR computations may be explained by the fact that the AGR computation creates smaller cells near the water surface, which results in larger local Courant numbers close to the free surface when the step size is fixed. The numerical scheme to solve the volume fraction is Courant number dependent, with high Courant numbers, the discretization scheme is less compressive: as the Courant number increases, the free-surface capturing scheme changes to a classical upwind scheme so that the free surface is smoothed.

For case 3b (Figure 18f), the ISIS-CFD (AGR) result shows a significant improvement both in the shape of the trough and the maximum depression when compared to the experimental results: at the midship location, the error is now approximately 0.3 millimetre (this was 0.75 for the ISIS-CFD result) and the shape shows better agreement with the experimental measurement. In addition, the unnatural peak in the water surface depression for the ISIS-CFD computation for this case is completely gone. The initial result from which the AGR case was restarted (ISIS-CFD c2) is shown with a light green colour in Figure 18f.

Influence of distance to the bank

When the distance between the ship hull and the bank decreases, lower pressures are generated on the starboard side of the ship and therefore the suction force towards the bank increases. This can be easily seen in Figure 19, which shows the pressure distribution on the hull and channel boundaries for three different distances to the vertical wall. The lower pressure area also results in an increase of the heeling moment. The change in yaw moment as a function of the distance to the bank is less pronounced. For the smallest bank distance, it can be seen that a significant low pressure area develops at the starboard side of the bow, which results in a change of the trend of the yaw moment.

Influence of water depth

As expected, a smaller water depth amplifies the low pressure area on the bottom of the hull, see Figure 20. Additionally, the blockage of the flow in the channel increases and more flow separation is found around the aft ship (see also the regions with low axial velocity shown in Figure 26 for case 3b with 35% under-keel clearance and Figure 24 for case 5b with 10% under-keel clearance). Due to the blockage, the flow is deflected around the model towards port side and the pressure at the port side of the model reduces. Additionally, a shift of the stagnation point on the bow to starboard is found. In the 50% UKC case, the side force is directed to the bank, but in reduced UKC conditions the low pressure area on port side and the high stagnation pressure on the starboard bow area result in a decrease of the side force. This was also found and discussed by L. Zou and Larsson (2013). Both

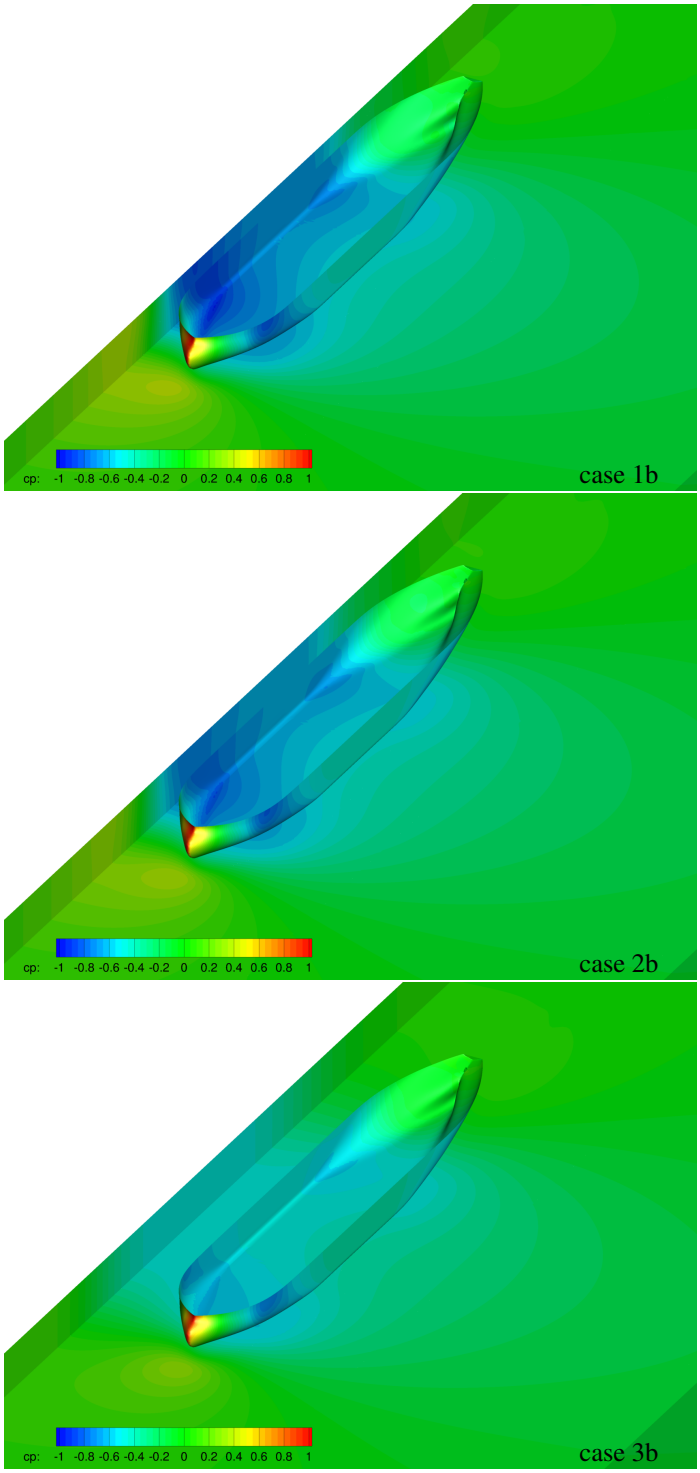

Figure 19: Pressure distribution on the hull as a function of distance from the vertical bank, REFRESCO

ISIS-CFD and REFRESCO predict that in the 10% UKC case the side force will even be directed away from the bank. This is however not confirmed by the measurements.

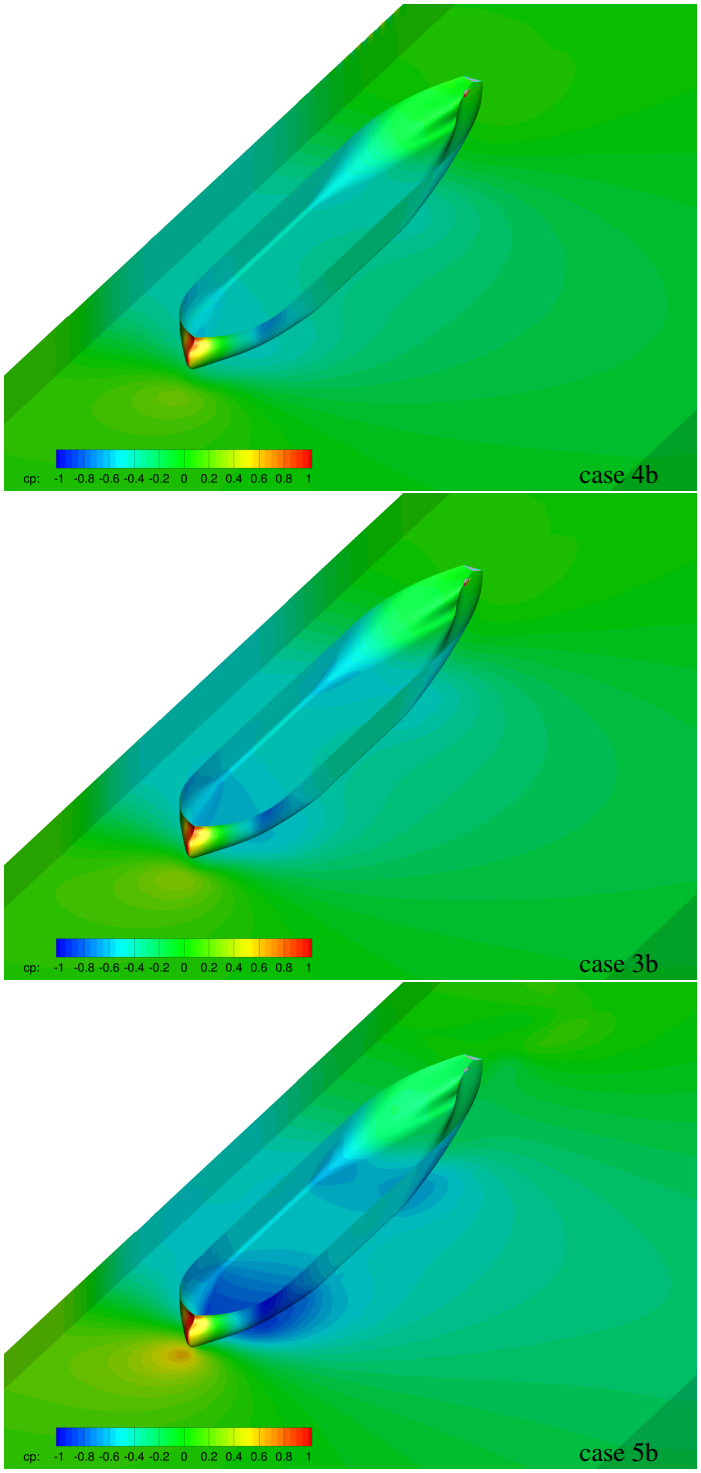

Figure 20: Pressure distribution on the hull as a function of water depth, ISIS-CFD

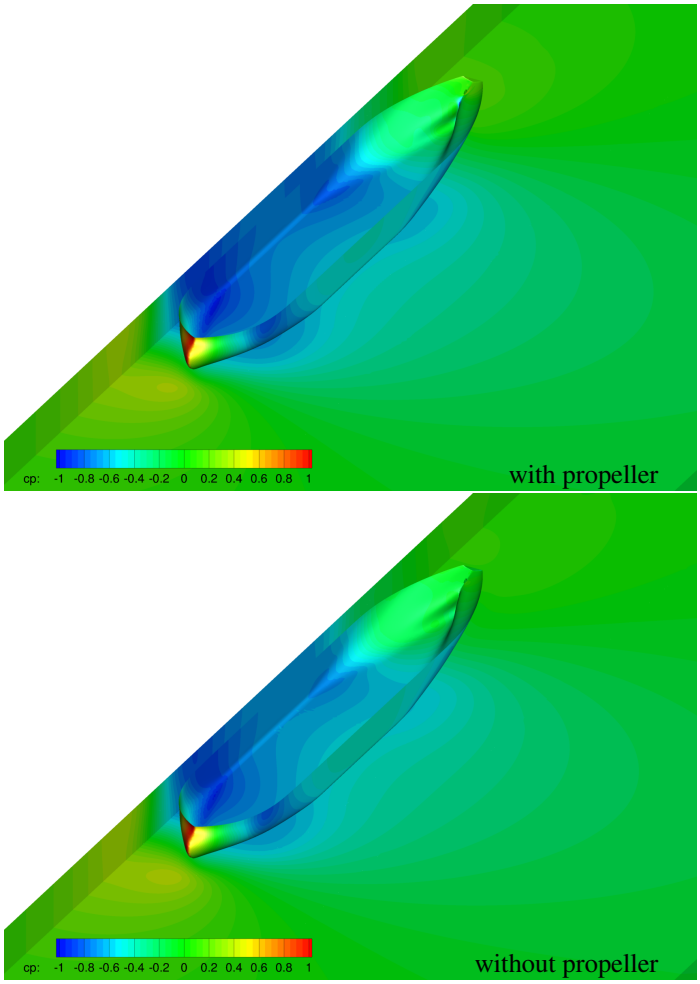

Figure 21: Case 1: Pressure distribution on the hull, REFRESCO

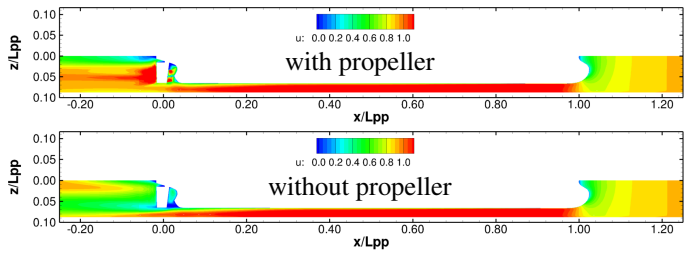

Figure 22: Case 1: Non-dimensional axial velocity distribution at centreline ($y = 0$), REFRESCO

Influence of propeller

In Figure 21, the pressure distribution on the hull, vertical wall and channel bottom is compared for the case with the smallest distance to the bank with (case 1a) and without (case 1b) propeller action. It is seen that the suction of the propeller accelerates the flow in the aft ship, leading to slightly lower pressures. This results in a slightly higher side force and more negative (pulling the stern to the wall) yaw moment, see Figure 12. Due to the propeller action, the flow does not separate as much as in the case without propeller and higher axial velocities are found in the area of the aft ship, see Figure 22. These findings agree with the conclusions from L. Zou and Larsson (2013).

Double body vs. free surface

The computations with REFRESCO have been done under the assumption that the free surface deformation does not strongly influence the results for this specific case. In the ISIS-CFD compu-

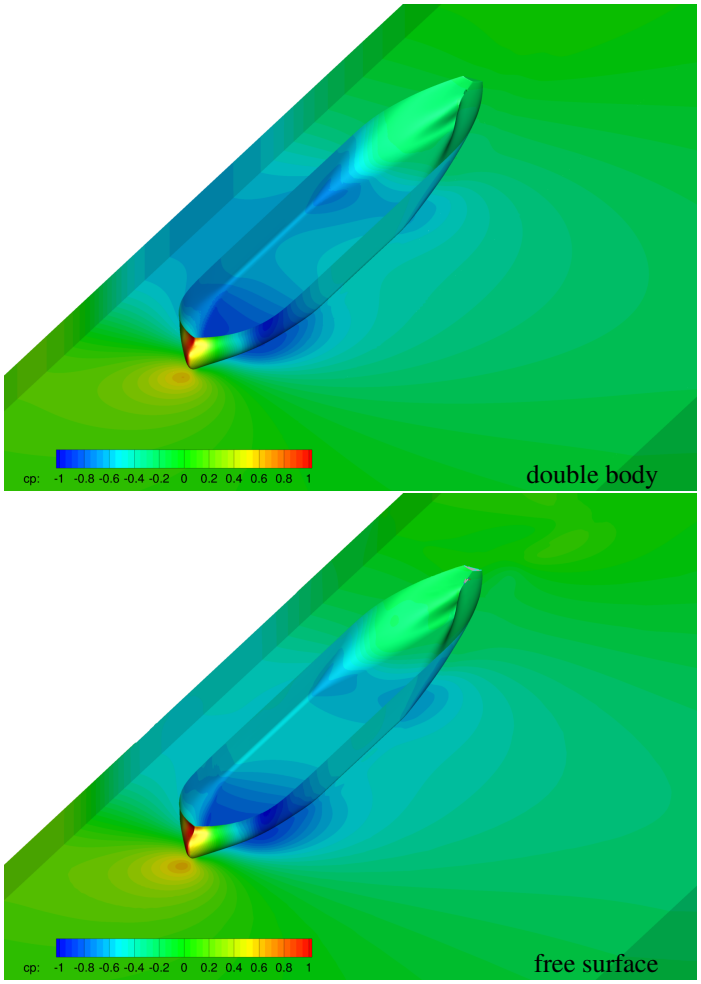

Figure 23: Case 5b: Pressure distribution on the hull, comparison between double body (REFRESCO) and free surface (ISIS-CFD) modelling

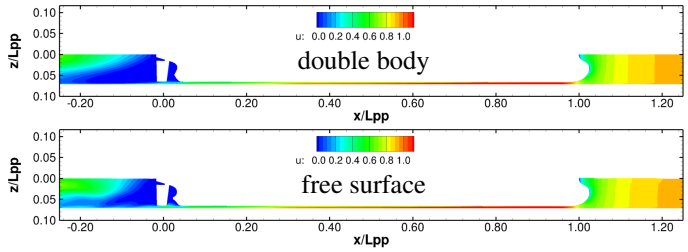

Figure 24: Case 5b: Non-dimensional axial velocity distribution at centreline ($y = 0$), comparison between double body (REFRESCO) and free surface (ISIS-CFD) modelling

tations performed by FHR and ECN/CNRS, the flow was resolved including the free surface effects. In Figure 23 and Figure 24, the results from REFRESCO are compared with the ISIS-CFD results obtained by FHR for case 5b. Case 5 has the smallest under-keel clearance and therefore the lowest water level in the channel and for this case the free surface effects are probably the largest, due to the largest blockage. From these figures, differences can be seen, showing especially a larger low-pressure area around midship in the double-body computation. It is therefore concluded that for this condition the free surface deformation may play a significant role. However, this case also exhibits a large area of flow separation (see the low velocity area behind the ship in Figure 24) and this introduces instationary flow. The difference therefore may also be caused by uncertainties in the results from the different solvers.

For a less severe case, case3b, the differences between the double body approach and the approach with free surface is less pronounced, see case 3b from REFRESCO in Figure 19 and from ISIS-CFD in Figure 20. Here, only small differences can be seen, which can be caused by differences due to the solver and grid, or by the use of the free surface. It is expected that for this case, with a relatively large distance to the bank and an intermediate water depth, the influence of the free surface modelling is not significant.

Effect of automatic grid refinement

In Figure 25 the differences in the pressure distribution obtained with the original grid and with automatic grid refinement is illustrated. Only around midship, small shifts in the contour lines are found. Also in the axial velocity distribution, see Figure 26, only small differences can be observed. Generally, it is concluded that the automatic grid refinement does not change the flow field drastically.

Potential flow vs. viscous flow

To investigate the discrepancy of the ROPES predictions with respect to the measurements and the results for the viscous-flow predictions, the pressure distribution on the hull predicted by ROPES and by REFRESCO are compared, see Figure 27. It is seen that on the starboard (bank-side) of the hull, lower pressures are predicted by ROPES than by REFRESCO. This results in a larger positive Y force, which is directed towards the bank. At the forward shoulder on port side, the low pressure trough is less in ROPES than in REFRESCO. Additionally, the pressure recovery in the aft ship is much more pronounced according to ROPES. Subsequently, a higher pressure area appears to exist at the starboard side of the stern. The differences in the pressure distribution computed by ROPES will induce a larger positive yawing moment (turning the bow towards the vertical bank). These observations confirm the discrepancies found in Figure 12. Apparently, when sailing close to a vertical bank, potential flow models will not be able to accurately predict the bank effects, and viscous-flow methods have to be adopted to obtain the right trends of bank suction or repulsion.

CONCLUSIONS

This paper presents new computational results of two viscous CFD codes and one potential code for bank effects. Experimental data was used to judge the ability of the computational tools to predict bank suction effects. From a large set of experimental data, five test cases were selected where two parameters were varied: a) the lateral distance to the bank and b) the under keel clearance. For each test case, two experiments were available:

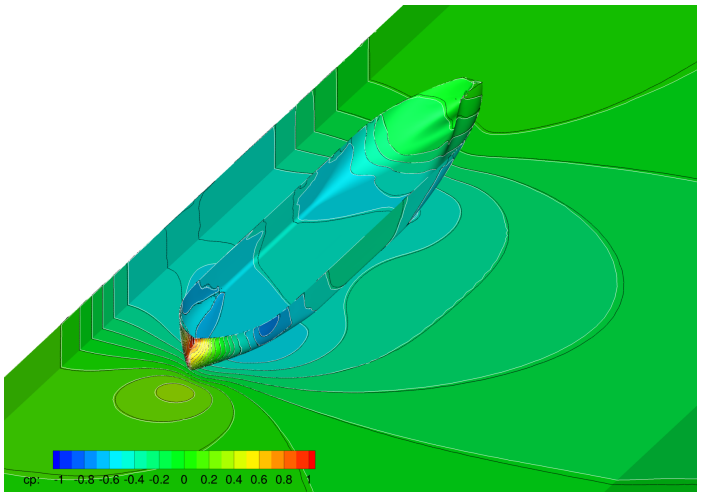

Figure 25: Case 3b: Pressure distribution on the hull, influence of automatic grid refinement (contour flood with white lines), compared with original grid results (black contour lines), ISIS-CFD

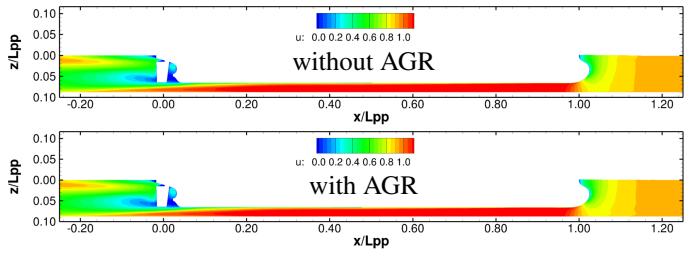

Figure 26: Case 3b: Non-dimensional axial velocity distribution at centreline ($y = 0$), influence of automatic grid refinement, ISIS-CFD

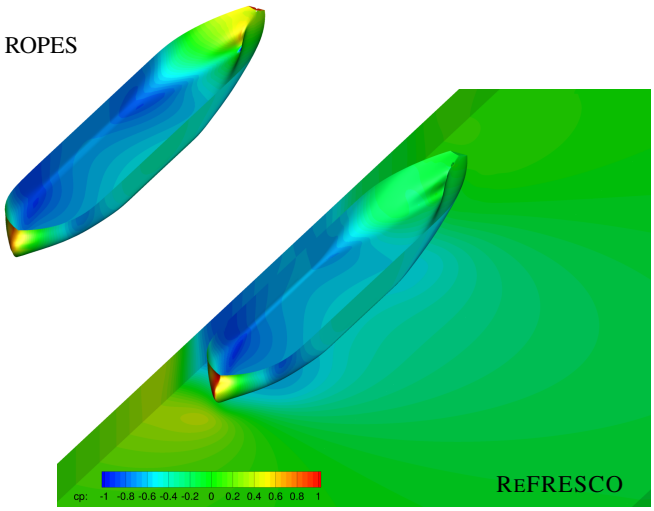

Figure 27: Case 1b: Pressure distribution on the hull, computed with ROPES (potential flow, pressure on bank and bottom has not been visualised here) and REFRESCO (viscous flow, *ultimatelyfine* grid)

the first one with propulsion and the second one with the propeller stopped. In total, 10 experimental conditions are used as reference. The experimental data was analysed for its convergence by computing the cumulative moving average, the cumulative standard deviation and the fast Fourier transform. In general, it was found that forces and moments show better convergence than sinkage and trim values. Ideally, experimental tests used as benchmark for evaluation of CFD methods should include uncertainties in the values that are computed by repeating each test condition multiple times. This was not the case for the current experimental data set, so values without uncertainties are used for comparison. In addition to the new results presented here, CFD data from literature is shown in the comparisons as well.

The grid convergence studies with REFRESCO and ISIS-CFD show that in order to obtain sufficiently low discretisation errors, very fine grids (with or without automatic grid refinement) are required.

Based on comparisons of the computations with experimental results, it is found that bank effects can be predicted using CFD tools. However, some deviation from the measurement is seen and this needs further study. Although the ISIS-CFD results with adaptive grid refinement indicate that improvements may be possible, other parameters need to be investigated as well. The majority of computations presented here were computed in steady mode. For the three computations that were executed in unsteady mode, small improvements were observed in the integral quantities. Furthermore, spurious oscillations of the water surface elevation that were observed in some of the steady computations, are not present in the unsteady computations (nor in the steady computations with automatic grid refinement). Comparisons of local flow quantities have shown that for ISIS-CFD results, the differences between steady and unsteady computations are very small. However, this is not conclusive as insufficient time was available to investigate e.g. the influence of the step size and convergence settings per step on the results. At the moment, it is not known whether a REFRESCO unsteady computation may alleviate the difficulties that were encountered in obtaining iteratively and statistically converged results using the steady approach. The specific turbulence model used may affect the results as well.

The effect of the propeller amplifies the bank effects, due to the reduction of pressures in the aft ship area and due to a change of the separation of the flow around the stern. To fully predict bank effects the propeller should therefore be incorporated in the computations. For the cases considered in this study, it is found that the consideration of free surface deformation does not significantly influence the predicted forces and moments, except for very small under keel clearance values.

The study also shows that for sailing close to a vertical bank in shallow water, potential flow models are not able to accurately predict the bank effects, and viscous-flow methods have to be adopted to obtain the right trends of bank suction or repulsion.

ACKNOWLEDGEMENTS

The work of MARIN has been performed in the context of the *TO2 (Toegepast Onderzoek Organisaties) Natte Kunstwerken van de Toekomst* project.

The work by ECN/CNRS was granted access to the HPC resources of IDRIS under the allocations 2014 and 2015 2a1308a made by GENCI (Grand Equipement National de Calcul Intensif).

REFERENCES

Bunnik, T. H. J. and Toxopeus, S. L. (2011). "Viscous flow effects of passing ships in ports". In: *30th International Conference on Ocean, Offshore and Arctic Engineering (OMAE)*. OMAE2011-49519. Rotterdam, The Netherlands. DOI: 10.1115/OMAE2011-49519.

Chen, H.-C., Liut, D. A., Hwang, W.-Y., and Lin, W.-M. (2003). "An advanced viscous flow computation method for ship-ship dynamic interactions in shallow and restricted waterway". In: *International Conference on Marine Simulation and Ship Manoeuvring (MARSIM)*. RC-35. The Society of Naval Architects of Japan and Japan Institute of Navigation. Kanazawa, Japan, pp. 1–10.

Dacles-Mariani, J., Zilliac, G. G., Chow, J. S., and Bradshaw, P. (1995). "Numerical/experimental study of a wingtip vortex in the near field". In: *AIAA Journal* 33.9, pp. 1561–1568. DOI: 10.2514/3.12826.

Dand, I. W. (1981). "On Ship-Bank Interaction". In: *RINA Spring Meeting*.

Delefortrie, G. (2015). *Accuracy of measurement devices for sinkage at the Flanders Hydraulics Research shallow-water towing tank*. Private communication.

Deng, G. B., Queutey, P., Vissoneau, M., and Salvatore, F. (2013). "Ship propulsion prediction with a coupled RANSE-BEM approach". In: *The V International Conference on Computational Methods in Marine Engineering. Marine 2013*. Marine 2013. (Hamburg, Germany). Ed. by B. Brinkmann and P. Wriggers.

Deng, G. B. and Visonneau, M. (1999). "Comparison of explicit algebraic stress models and second-order turbulence closures for steady flow around ships". In: *7th Symposium on Numerical Ship Hydrodynamics*. (Nantes, France). DOI: 10.1.1.534.5953.

Eça, L. and Hoekstra, M. (2009). "Evaluation of numerical error estimation based on grid refinement studies with the method of the manufactured solutions". In: *Computers & Fluids* 38.8, pp. 1580–1591. DOI: 10.1016/j.compfluid.2009.01.003.

Eça, L. and Hoekstra, M. (2014). "A procedure for the estimation of the numerical uncertainty of CFD calculations based on grid refinement studies". In: *Journal of Computational Physics* 262, pp. 104–130. DOI: 10.1016/j.jcp.2014.01.006.

Guilmineau, E., Chikhaoui, O., Deng, G. B., and Visonneau, M. (2013). "Cross wind effects on a simplified car model by a DES approach". In: *Computers & Fluids* 78, pp. 29–40. DOI: 10.1016/j.compfluid.2011.08.020.

Klaij, C. M. and Vuik, C. (2013). "SIMPLE-type preconditioners for cell-centered, colocated finite volume discretization of incompressible Reynolds-averaged Navier-Stokes equations". In: *International Journal for Numerical Methods in Fluids* 71.7, pp. 830–849. DOI: 10.1002/fld.3686.

Korsmeyer, F. T., Lee, C.-H., and Newman, J. N. (1993). "Computation of Ship Interaction Forces in Restricted Waters". In: *Journal of Ship Research* 37.4, pp. 298–306.

Lataire, E., Vantorre, M., and Delefortrie, G. (2012). "A prediction method for squat in restricted and unrestricted rectangular fairways". In: *Ocean Engineering* 55.55, pp. 71–80. DOI: 10.1016/j.oceaneng.2012.07.009.

Leroyer, A. and Visonneau, M. (2005). "Numerical methods for RANSE simulations of a self-propelled fish-like body". In: *Journal of Fluids and Structures* 20 (7), pp. 975–991. DOI: 10.1016/j.jfluidstructs.2005.05.007.

Lo, D. C., Su, D.-T., and Lin, I.-F. (2009). "Applying Computational Fluid Dynamics to Simulate Bank Effects". In: *Nineteenth International Offshore and Polar Engineering Conference*. Osaka, Japan, pp. 466–471.

Menter, F. R. and Egorov, Y. (2005). "A Scale-Adaptive Simulation Model using Two-Equation Models". In: AIAA 2005-1095. American Institute of Aeronautics and Astronautics.

Menter, F. R., Kuntz, M., and Langtry, R. (2003). "Ten Years of Industrial Experience with the SST Turbulence Model". In: *Turbulence, Heat and Mass Transfer 4*, pp. 625–632.

Pereira, F. S., Vaz, G., and Eça, L. (2014). "On the use of Hybrid Turbulence Models". In: *17th Numerical Towing Tank Symposium (NuTTS)*. Marstrand, Sweden, pp. 135–140.

Pinkster, J. A. (2004). "The Influence of a Free Surface on Passing Ship Effects". In: *International Shipbuilding Progress* 51.4, pp. 313–338.

Pinkster, J. A. and Bhawsinka, K. (2013). "A real-time simulation technique for ship-ship and ship-port interactions". In: *The 28th international Workshop on Water Waves and Floating Bodies (IWWWFB)*.

Queutey, P. and Visonneau, M. (2007). "An interface capturing method for free-surface hydrodynamic flows". In: *Computers & Fluids* 36 (9), pp. 1481–1510. DOI: 10.1016/j.compfluid.2006.11.007.

Rijpkema, D. R., Starke, A. R., and Bosschers, J. (2013). "Numerical simulation of propeller-hull interaction and determination of the effective wake field using a hybrid RANS-BEM approach". In: *Third International Symposium on Marine Propulsors (SMP)*. Launceston, Tasmania, Australia.

Tuck, E. O. and Newman, J. N. (1974). "Hydrodynamic interactions between ships". In: *10th Symposium on Naval Hydrodynamics*. Office of Naval Research, pp. 35–51.

Van Kerkhove, G., Vantorre, M., and Delefortrie, G. (2009). "Advanced model testing techniques for ship behaviour in shallow and confined water". In: *Proceedings of AMT*, p. 29. URL: http://www.vliz.be/imisdocs/publications/153758.pdf.

Vantorre, M. and Laforce, E. (1998). "Experimental investigation of hydrodynamic forces acting on a ship in the vicinity of a quay wall". In: *MAN'98 International Symposium and Work-*

shop on Forces Acting on a Manoeuvring Vessel. Val de Reuil, France.

Vaz, G., Jaouen, F. A. P., and Hoekstra, M. (2009). "Free-Surface Viscous Flow Computations. Validation of URANS Code FRESCO". In: *28th International Conference on Ocean, Offshore and Arctic Engineering (OMAE)*. OMAE2009-79398. Honolulu, Hawaii. DOI: 10.1115/OMAE2009-79398.

Vaz, G. and Bosschers, J. (2006). "Modelling of three dimensional sheet cavitation on marine propellers using a boundary element method". In: *Sixth International Symposium on Cavitation (CAV)*. Wageningen, The Netherlands.

Wackers, J., Deng, G. B., Leroyer, A., Queutey, P., and Visonneau, M. (2014). "Combined refinement criteria for anisotropic grid refinement in free-surface flow simulation". In: *Computers and Fluids* 92, pp. 209–222. DOI: 10.1016/j.compfluid.2013.12.019.

Wackers, J., Deng, G. B., Leroyer, A., Queutey, P., Visonneau, M., Palmieri, A., and Liverani, A. (2015). "Can Adaptive Grid Refinement Produce Grid-Independent Solutions for Complex Flows?" In: *VII International Conference on Adaptive Modeling and Simulation*. ADMOS 2015. (Nantes, France). Ed. by F. Chinesta, L. Chamoin, and P. Diez.

Xiang, X. and Faltinsen, O. M. (2010). "Maneuvering of Two Interacting Ships in Calm Water". In: *11th International Symposium on Practical Design of Ships and Other Floating Structures (PRADS)*. Rio de Janeiro, Brazil.

Yeung, R. W. and Tan, W. T. (1980). "Hydrodynamic interactions of ships with fixed obstacles". In: *Journal of Ship Research* 24.1, pp. 50–59.

Zhou, M. and Zou, Z. (2013). "Numerical study on the influences of canal geometry on ship squat". In: *Scientific Journals of the Maritime University of Szczecin* 36.1, p. 5. ISSN: 1733-8670. URL: http://repository.am.szczecin.pl/handle/123456789/554 (visited on 08/14/2015).

Zou, L. and Larsson, L. (2013). "Confined water effects on the viscous flow around a tanker with propeller and rudder". In: *International Shipbuilding Progress* 60.1–4, pp. 101–125. DOI: 10.3233/ISP-130101.

Zou, L. (2012). "CFD Predictions Including Verification and Validation of Hydrodynamic Forces and Moments on Ships in Restricted Waters". PhD thesis. Gothenburg, Sweden: Chalmers University of Technology, Department of Shipping and Marine Technology.

Zou, L., Larsson, L., Delefortrie, G., and Lataire, E. (2011). "CFD Prediction And Validation Of Ship-Bank Interaction In A Canal". In: *2nd International Conference on Ship Manoeuvring in Shallow and Confined Water: Ship to Ship Interaction*. Trondheim, Norway.